

Finite Difference Time Domain Based Investigation of the Light Transmission Characteristics of Strongly Disordered Systems Mimicking Self-organized Nanowire Arrays

by

Md. Ishfak Tahmid
Student ID: 0419062206

A thesis submitted in partial fulfillment of the requirements of the
degree of
Master of Science in Electrical and Electronic Engineering




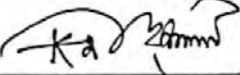
Department of Electrical and Electronic Engineering
Bangladesh University of Engineering and Technology (BUET)
Dhaka, Bangladesh

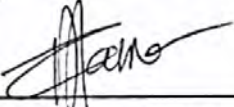
June 28, 2022

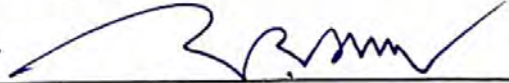
The thesis titled "Finite Difference Time Domain Based Investigation of the Light Transmission Characteristics of Strongly Disordered Systems Mimicking Self-organized Nanowire Arrays" submitted by Md. Ishfak Tahmid, Student ID: 0419062206, Session: April 2019 has been accepted as satisfactory in partial fulfillment of the requirement for the degree of Masters of Science in Electrical and Electronic Engineering on June 28, 2022.


BOARD OF EXAMINERS

1. 
Chairman
(Supervisor)

Dr. Md. Zunaid Baten
Associate Professor
Department of Electrical and Electronic Engineering
Bangladesh University of Engineering and Technology
Dhaka, Bangladesh.
2. 
Member
(Ex-Officio)

Dr. Md. Kamrul Hasan
Professor and Head
Department of Electrical and Electronic Engineering
Bangladesh University of Engineering and Technology
Dhaka, Bangladesh.
3. 
Member

Dr. Sharif Mohammad Mominuzzaman
Professor
Department of Electrical and Electronic Engineering
Bangladesh University of Engineering and Technology
Dhaka, Bangladesh.
4. 
Member

Dr. Mohammad Faisal
Professor
Department of Electrical and Electronic Engineering
Bangladesh University of Engineering and Technology
Dhaka, Bangladesh.
5. 
Member
(External)

Dr. Md. Abdullah Zubair
Associate Professor
Department of Glass and Ceramic Engineering
Bangladesh University of Engineering and Technology
Dhaka, Bangladesh.

Declaration

It is hereby declared that this thesis or any part of it has not been submitted elsewhere for the award of any degree or diploma.

Signature of the student

Md. Ishfak Tahmid

(Md. Ishfak Tahmid)

*This thesis is dedicated to my loving parents and
respected teachers*

Acknowledgement

To begin, I would like to express my profound gratitude to the Almighty for providing me the opportunity to complete my Thesis. I am also grateful to my parents, friends, and family for always believing in me.

I would also like to convey my heartfelt thanks to my thesis advisor, Dr. Md. Zunaid Baten, for his constant support and guidance throughout the completion of the work. I will always be indebted to him for igniting the spirit of research in me. His consistent sharing of knowledge and discussion of ideas helped me immensely in every step of this work. I also specifically thank him for taking proactive steps to complete this thesis work on time, despite the fact that the epidemic continued to spread over the world. I will remember the memories of working with him for the rest of my life.

I would also like to thank Dip Joti Paul for his suggestions and knowledge sharing to advance this thesis work.

I also thank the members of my thesis committee, Dr. Md. Kamrul Hasan, Dr. Sharif Mohammad Mominuzzaman, Dr. Mohammad Faisal and the external member Dr. Md. Abdullah Zubair.

Md. Ishfak Tahmid

June 28, 2022

Abstract

In this study, we have investigated the effects of introducing randomness on the transmission characteristics of light in dielectric nanowire arrays. Periodic, correlated weakly disordered, correlated strongly disordered, and uniform random (uncorrelated disordered) systems are studied using finite difference time domain (FDTD) analysis technique. Upon analyzing the origin of transmission gaps in such arrays, it is found that both Bragg and Mie process are involved in the gap formation process. The shrinkage of gap in disordered arrays confirms the involvement of Bragg process and the sustenance of gap in completely random arrays is an indication of the involvement of Mie process. We have also found that transmission gap can be tuned in random arrays similar to the case in periodic arrays by varying nanowire diameter and fill-factor of the arrays. Red-shifting of the gap with an increase in diameter and blue-shifting for an increase in fill-factor is observed in both periodic and random systems. Again, transmission in the passband region is found to decrease for arrays with higher degree of disorder because of increased scattering in such arrays. We have also proposed optimized designs of power splitters and wavelength demultiplexers that are optimized for passband wavelengths (550 nm and 650 nm). We have found that inverse design based optimization technique can be applied on both periodic and random nanowire arrays to get comparable performance by generating customized designs. Thus, our study will advance the field of disorder photonics by creating scopes for employing disordered systems to realize photonic waveguides and integrated circuits.

Contents

Declaration	iii
Acknowledgement	iv
List of Figures	viii
List of Tables	xiii
1 Introduction	2
1.1 Preface	2
1.2 Literature review	3
1.3 Motivation of the Work	6
1.4 Objectives of the Work	7
1.5 Outline of the Thesis	7
2 Theoretical Background	9
2.1 The Maxwell Equations	9
2.2 Photonic Crystals	10
2.3 2D Photonic Crystals	10
2.3.1 Photonic band structure	11
2.3.2 Photonic bandgap	12
2.3.3 Origin of photonic bandgap	12
2.4 Light Scattering	13
2.4.1 Rayleigh Scattering	14
2.4.2 Bragg scattering	15
2.4.3 Mie scattering	16
3 Analyzed Structures and Computational Methods	17

3.1	Self-organized Growth of Nanowire Array	17
3.2	Device Structure	20
3.2.1	Periodic nanowire array	20
3.2.2	Correlated random array	21
3.2.3	Uniform random array	22
3.3	Photonic Band-structure of Periodic Array	23
3.4	Finite Difference Time Domain Analysis	24
3.4.1	Simulation details	24
3.4.2	Benchmarking with band-structure	26
3.5	Inverse Design-based Optimization	27
3.5.1	Algorithm	27
3.5.2	Initial structure	28
3.5.3	Optimization	28
3.5.4	Discretization	30
3.5.5	FDTD simulation	31
4	Results and Discussion	32
4.1	Light Transmission Characteristics	32
4.1.1	Origin of transmission gap	32
4.1.2	Transmission gap tuning	36
4.1.2.1	Effects of variation in diameters	36
4.1.2.2	Effects of variation in fill-factors	39
4.1.3	Effects of system length	42
4.1.3.1	Comparison of transmittance	42
4.1.3.2	Light scattering	43
4.2	Disorder System Based Demultiplexers and Power Splitters	45
4.2.1	Power splitters at 550 nm wavelength	46
4.2.2	Power splitters at 650 nm wavelength	49
4.2.3	WDM at 550 and 650 nm wavelengths	52
5	Conclusion	59
5.1	Summary	59
5.2	Future Scopes	60

List of Figures

1.1	SEM image of hole type 2D photonic crystal with hole size of 240 nm diameter. Inset shows the top view of such photonic crystal having 170 nm hole diameter [1].	4
1.2	PBG like transmission gap in penrose type quasi-crystal [2].	5
2.1	Schematics of 1D, 2D and 3D photonic crystals [3].	10
2.2	A schematic representation of 2D photonic crystal consisted of dielectric columns suspended in air. The square shape unit cell is also shown where lattice constant is denoted by a and radius of the nanowires is denoted by r [3].	11
2.3	The photonic bandstructure of a 2D PC consisted of square shape unit cell of dielectric cylinders suspended in air. The unit cell and the Brillouin zone are shown in the inset. The irreducible Brillouin zone is marked with the blue triangle [3].	12
2.4	Displacement field distributions at high symmetric X and M points of the irreducible Brillouin zone for TM polarization [3].	13
2.5	Elastic scattering of light by a particle [4].	14
2.6	Rayleigh scattering and Mie scattering [5].	15
2.7	Constructive and destructive interference due to Bragg process in a crystal [6].	16
3.1	Growth process of GaN nanowire on Si substrate [7].	18
3.2	SEM images of GaN nanowires grown with Ga fluxes of (a) 3×10^{-8} , (b) 7.8×10^{-8} , and (c) 9×10^{-8} Torr [8].	19

3.3	(a) SEM image of the top view of MBE grown self-organized GaN nanowires on Si; (b) transferred pattern generated through image processing; (c) A 3D schematic diagram of GaN nanowire array and (d) corresponding 2D cross-section in the x-y plane [9].	19
3.4	Cross-sectional view of a $3 \times 3 \mu\text{m}^2$ periodic array with 50 % ff having identical nanowires of 60 nm diameter.	20
3.5	Maximum achievable disorder strength (ζ) for different allowed variation. Square shape unit cell of the periodic array is shown in the inset. . .	21
3.6	Cross-sectional views of (a) correlated weakly disordered ($\zeta = 0.1425$) and (b) correlated strongly disordered ($\zeta = 0.9963$) arrays with 50 % ff having identical nanowires of 60 nm diameter.	22
3.7	Cross-sectional view of a $3 \times 3 \mu\text{m}^2$ uniform random array with 50 % ff having identical nanowires of 60 nm diameter.	23
3.8	TE and TM Band structures of the periodic NW array. The irreducible Brillouin zone for the square shape unit cell is marked with a blue triangle in the inset.	24
3.9	Yee lattice in a 3D computational space [10].	25
3.10	Transmittance (T) and reflectance (R) spectra of periodic GaN nanowire array with 70 nm diameter and 50 % ff for both TE and TM modes. .	26
3.11	Periodic nanowire array initial structure. Design region is marked with red dotted region. Source is injected along left port marked as “3” and output is recorded along right ports marked as “1” and “2”.	28
3.12	Random nanowire array initial structure.	29
3.13	Flow chart of the steps to be followed to design a photonic device using inverse design technique [11].	30
4.1	Transmittance spectra for periodic, correlated disordered, and uniform random systems with 50 % ff and 60 nm diameter.	33
4.2	Reflectance and transmittance spectra for uniform random systems. Here, configurational average of four different random configurations with identical diameter and ff of 70 nm and 50 % are shown.	34

4.3	Relative bandgap (χ) as a function of disorder strength (ζ) for correlated disordered arrays. Percentage of Bragg contribution in bandgap formation process is also shown.	35
4.4	Contour plot of transmittance in periodic arrays for different diameters of the nanowires. Fill-factor is kept constant at 50 % in each case. . .	36
4.5	Contour plot of transmittance in random arrays for different diameters of the nanowires. Fill-factor is kept constant at 50 % in each case. . .	37
4.6	Variation of center wavelength of the transmission gap and gap-midgap ratio as a function of diameters for both periodic and random arrays.	37
4.7	Scattering in periodic arrays for different diameters of the nanowires. Fill-factor is kept constant at 50 % in each case.	38
4.8	Scattering in random arrays for different diameters of the nanowires. Fill-factor is kept constant at 50 % in each case.	39
4.9	Transmittance spectra of periodic arrays at different fill-factors with the diameter being fixed at 70 nm in each case.	40
4.10	Transmittance spectra of random arrays at different fill-factors with the diameter being fixed at 70 nm in each case.	41
4.11	Variation of center wavelength of the transmission gap and gap-midgap ratio as a function of fill-factors for both periodic and random arrays.	41
4.12	Transmittance spectra at different system lengths (L) for both periodic and random systems.	42
4.13	Scattering spectra at different system lengths (L) for periodic systems. The location of scattering monitors to record the scattered flux is also shown in the inset.	43
4.14	Scattering spectra at different system lengths (L) for random systems.	44
4.15	Optimized power splitter for 550 nm wavelength with periodic nanowire array initial structure.	44
4.16	Discretized power splitter for 550 nm wavelength with periodic nanowire array initial structure.	45
4.17	Electric field distribution at 550 nm wavelength of the designed power splitter with periodic nanowire array initial structure.	45

4.18	Transmittance spectra for the designed power splitter with periodic nanowire array initial structure.	46
4.19	Optimized power splitter for 550 nm wavelength with random nanowire array initial structure.	46
4.20	Discretized power splitter for 550 nm wavelength with random nanowire array initial structure.	47
4.21	Electric field distribution at 550 nm wavelength for the designed power splitter with random nanowire array initial structure.	47
4.22	Transmittance spectra for the designed power splitter with random nanowire array initial structure.	48
4.23	Optimized power splitter for 650 nm wavelength with periodic nanowire array initial structure.	48
4.24	Discretized power splitter for 650 nm wavelength with periodic nanowire array initial structure.	49
4.25	Electric field distribution at 650 nm wavelength of the designed power splitter with periodic nanowire array initial structure.	49
4.26	Transmittance spectra for the designed power splitter with periodic nanowire array initial structure.	50
4.27	Optimized power splitter for 650 nm wavelength with random nanowire array initial structure.	50
4.28	Discretized power splitter for 650 nm wavelength with random nanowire array initial structure.	51
4.29	Electric field distribution at 650 nm wavelength for the designed power splitter with random nanowire array initial structure.	51
4.30	Transmittance spectra for the designed power splitter with random nanowire array initial structure.	52
4.31	Optimized demultiplexer structure for periodic nanowire array initial structure.	53
4.32	Discretized demultiplexer structure for periodic nanowire array initial structure.	54

4.33	Electric field distributions at 550 nm (top) and 650 nm (bottom) wavelengths for the designed demultiplexer with periodic nanowire array initial structure.	54
4.34	Transmittance spectra for the designed demultiplexer with periodic nanowire array initial structure.	55
4.35	Optimized demultiplexer structure for random nanowire array initial structure.	55
4.36	Discretized demultiplexer structure for random nanowire array initial structure.	56
4.37	Electric field distributions at 550 nm (top) and 650 nm (bottom) wavelengths for the designed demultiplexer with random nanowire array initial structure.	56
4.38	Transmittance spectra for the designed demultiplexer with random nanowire array initial structure.	57

List of Tables

- 4.1 Comparison of transmittance for the designed power splitters. 53
- 4.2 Comparison of transmittance for the designed wavelength demultiplexers. 57

List of Abbreviations

FDTD	Finite Difference Time Domain
WDM	Wavelength Demultiplexers
PBG	Photonic Bandgap
SEM	Scanning Electron Microscope
MBE	Molecular Beam Epitaxy

Chapter 1

Introduction

1.1 Preface

Controlling the propagation and localization of light has been an integral part of the research on photonic devices and systems. In this regard, the invention of photonic crystals (PCs) by Eli Yablonovitch offered ample scopes to the researchers to manipulate the confinement and transmission of photons in a medium consisting of periodic variation of dielectric constant [12]. In the direction of periodic variation, electromagnetic wave of particular frequency band is not allowed to propagate through the structure called photonic bandgap (PBG). As a result, a gap also appears in the corresponding transmission spectra of the structure. Tuning this transmission gap based on structural engineering is, therefore, a specific field of investigation to the scientific community. In particular, 2D photonic crystals (PCs) are in the focus of attention due to its mature fabrication process and wide variety of control over light propagation as transverse electric (TE) and transverse magnetic (TM) polarized light behavior is completely different in 2D PCs [13, 14]. Consequently, the design and fabrication of 2D PCs are being studied experimentally and theoretically for a broad range of application in optical field, which includes LEDs, LASERs, photovoltaics, and high Q cavities [15–22].

Again, recent studies on quasi-periodic and correlated disordered structures have revealed that photonic band-gap can be found even in the absence of structural periodicity [23–25]. This discovery has added a new dimension for the researchers in the area of disordered photonics where random structures are analyzed to get

significant characteristics compared to periodic counterpart. This phenomenal characteristic has already been used to implement disordered structures for the realization of cavity resonators, randomly distributed feedback lasers and light harvesting in solar cells [26, 27]. In this regard, investigating the light transmission characteristics in random arrays of dielectric scatterers is an interesting area of exploration. Hence, a detailed investigation of strongly disordered arrays will enhance the understanding of light transmission characteristics and will eventually lead to the utilization of such structures in advanced optoelectronic and photonic applications. Again, with the development of computational facility, inverse design-based optimization of photonic integrated circuits has opened the door for getting user specified outputs with customized designs [28, 29]. So, by blending the understanding of light transmission in disordered arrays with inverse design technique, wavelength demultiplexers and power splitters can be devised based on random structures.

1.2 Literature review

Photonic crystals, after being introduced for the first time by Yablonovitch, have been in the focus of attention of the research community due to providing the opportunity for controlling the transmission and confinement of light through structural modifications [12, 30–33]. As a result, numerous studies have been conducted to understand the origin and behavior of photonic bandgap in such periodic structures [34, 35]. Though complete photonic bandgap can only be easily obtained in 3D PCs, analysis on such crystals are limited due to complex fabrication process. In this regard, mature fabrication process of 2D PCs provide design flexibility to the researchers and thus offering ample scopes for investigating such crystals. Precisely controlling the dielectric constants of constituent materials, 2D PCs can be designed to possess only TE or TM bandgaps [13, 14]. Dielectric rods suspended in air and air holes in a dielectric are two of the most commonly analyzed types of 2D PCs. Whereas TM bandgap is generally found in the first type, TE bandgap is more likely to be obtained in the later [3]. This is due to the difference in the concentration of electric fields in the dielectric and the air regions. So recent

studies are conducted on the modulation of band-gap of 2D PCs. Caro *et al.* [1] studied hole type PCs, whereas melo *et al.* [36] reported the effects of lattice structure and geometry of dielectric column variation on the existence of band-gap. SEM image of hole type 2D PCs studied by Caro *et al.* [1] is shown in Fig. 1.1.

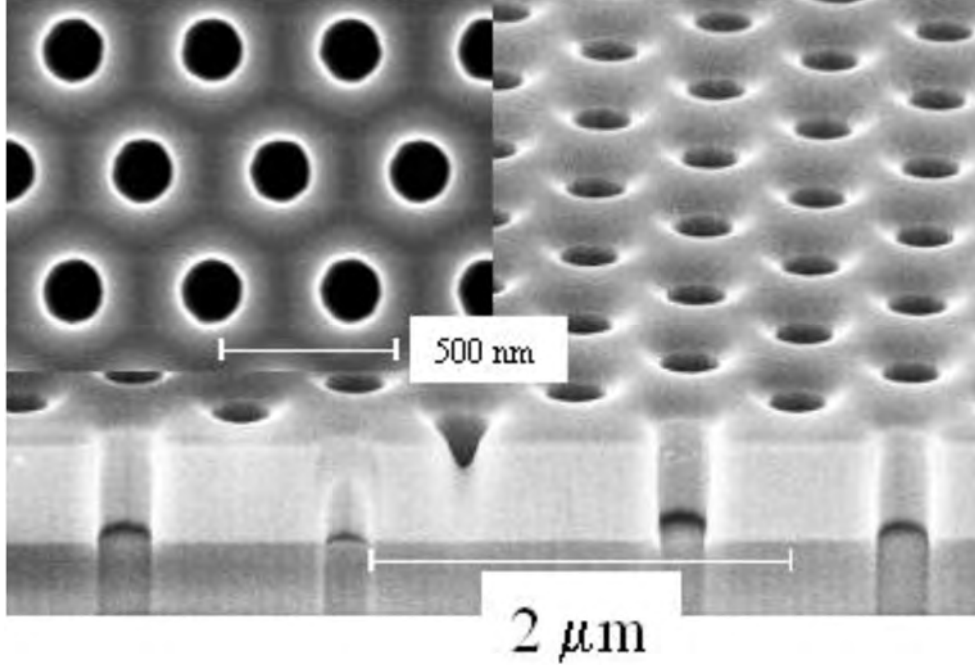


Figure 1.1: SEM image of hole type 2D photonic crystal with hole size of 240 nm diameter. Inset shows the top view of such photonic crystal having 170 nm hole diameter [1].

Though PBGs in periodic systems are investigated in detail, the effects of introducing randomness on the characteristics of PBG is less explored. However, recent studies on disordered arrays have revealed that PBG is not a unique characteristics of periodic array only. Rather the signature of PBG can also be found in quasi-periodic and correlated disordered structures [23–25, 37]. Chan *et al.* [25] and Wang *et al.* [24] reported the existence of PBG in 2D photonic quasi-crystals where the collective effects of multiple scattering occurring from the quasi-periodic variation of dielectric constant results in the formation of PBG. Multiple scattering assisted PBG is also reported by Della *et al.* [23] for penrose-type quasi-crystals. Bayindir *et al.* [2] reported such appearance of PBG like transmission gap in a penrose type quasi-crystal which is shown in Fig. 1.2.

Again, arranging the scatterers in a quasi-crystals in a hyperuniform pattern and bridging the adjacent scatterers with thin lines, complete PBG is obtained by

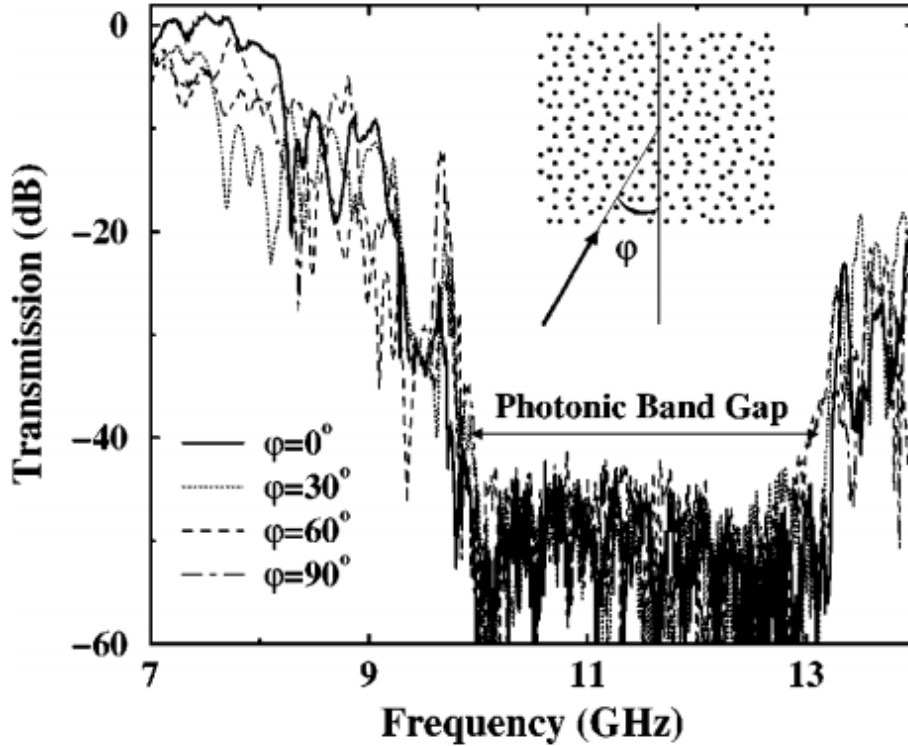


Figure 1.2: PBG like transmission gap in penrose type quasi-crystal [2].

Florescu *et al.* even in 2D PCs to impede the flow of both TE- and TM-polarized light [38, 39]. Near-zero transmission regions, resembling PBG, is also reported for weakly disordered systems where randomness is introduced in correlation with the corresponding periodic systems [37, 40]. Based on a theoretical analysis on such correlated weakly disordered systems, Nojima *et al.* attributed Bragg and Mie process to be involved in the gap formation process [41]. Though the characteristics of PBG in periodic, quasiperiodic, and correlated weakly disordered structures are studied in detail, the prospect of strongly disordered systems with uniform (uncorrelated) randomness in showing the signature of such PBG-like transmission gaps remained unexplored. Also the prospect of utilizing such uniform random systems for designing photonic components like waveguides, couplers, power splitters and beam-splitters has remained unattended- a study that deserves detailed investigation for realizing disordered system based future photonic integrated circuits.

1.3 Motivation of the Work

Though ordered NW arrays are investigated thoroughly, the absence of orderliness in self-organized growth of dielectric NW arrays has inspired us to investigate the possibility of getting transmission gaps in such uniform random systems similar to the case of periodic or quasi-periodic systems. Such arrays have already garnered the attention of the research community as they can be easily grown using molecular beam epitaxy (MBE) and can be utilized for the realization of optoelectronic and photonic devices [42, 43]. Consequently, detectors and lasers with a wide operating range from UV to near infrared regime have been realized experimentally based on such self-organized GaN NWs [44–48]. Moreover, Hazari *et al.* [49] utilized III-nitride NWs grown on (001) silicon substrate for the realization of photonic integrated circuits. Again, the capability to tune Anderson localized resonant modes by varying areal density and diameters of the NWs in such disordered arrays, reported in a recent study, piqued our interest to investigate the tuning possibility of transmission gaps in such uniform random systems [9].

Again, inverse design technique has recently emerged as an efficient method to generate customized structural design for getting optimized and user-specified output. As structural modification-based conventional optimization methods are both time and cost ineffective, inverse design technique holds promise for efficient optimization of advanced photonic devices [50–53]. In this regard, blending the understanding of light transmission in disordered arrays with inverse design technique for optimizing GaN NW array-based nano-photonic waveguides is an interesting area of exploration.

Again, the growth of perfectly periodic nanowire arrays requires sophisticated and expensive process and tools. Recently, periodic III-V semiconductor arrays have been grown on SiO₂ by employing electron beam lithography (EBL) technique [54]. Perfectly periodic 2D photonic crystals and silicon nanopillar array are also reported to be fabricated based on EBL technique [55, 56]. However, the setup, operation, and maintenance cost of electron beam lithography is very expensive. But, the growth of nanowire array by using molecular beam epitaxy (MBE) is relatively cost-effective. Though the growth of perfectly periodic arrays is not possible using MBE, self-organized growth of nanowire array is possible. Nanowire

arrays grown in this self-organized process are observed to have completely random pattern. So, if comparable performance as periodic arrays can be obtained with such random arrays, then low-cost photonic devices with comparable performance can be fabricated. As a result, this study aims to investigate the transmission characteristics of random nanowire arrays and the possibility of designing photonic devices based on such arrays.

1.4 Objectives of the Work

The objectives of this thesis are the following:

- To study the light transmission characteristics of uniform random media representing self-organized nanowire arrays of different areal densities and diameters.
- To compare the transmission characteristics of strongly disordered systems with those of periodic, quasi-periodic and weakly-disordered ones.
- To explore the prospect of tuning the transmission characteristics of strongly disordered media for possible applications as photonic waveguide.
- To design and analyze de-multiplexers and power-splitters considering self-organized nanowire array based disordered systems.

1.5 Outline of the Thesis

Chapter 2 represents a short theoretical discussion that is needed to better understand this thesis work.

Chapter 3 provides a detailed discussion on the research methodology and the analyzed structures. The simulation techniques and tools employed in this thesis are also discussed in this section.

Chapter 4 includes all the simulation results with associated graphs, plots, and tables. Detailed explanation of the results obtained is also discussed in this section.

Chapter 5 concludes the thesis by summarizing the results and discussing the future scopes of the study.

Chapter 2

Theoretical Background

In this chapter, a brief overview of the theory of light transmission in dielectric array is discussed. The concept of photonic crystals and photonic bandgap in periodic dielectric arrays are also introduced in this chapter.

2.1 The Maxwell Equations

Having a thorough understanding of Maxwell's equations is a must for investigating light transmission characteristics in a medium. The electric field intensity, electric flux density, magnetic flux density, and magnetic field intensity being denoted by \mathbf{E} , \mathbf{D} , \mathbf{B} , and \mathbf{H} respectively, Maxwell equations can be represented as follows:

$$\nabla \cdot \mathbf{D} = \rho \quad (2.1)$$

$$\nabla \cdot \mathbf{B} = 0 \quad (2.2)$$

$$\nabla \times \mathbf{E} = -\frac{\partial \mathbf{B}}{\partial t} \quad (2.3)$$

$$\nabla \times \mathbf{B} = \mu_0 \mathbf{J} + \varepsilon_0 \mu_0 \frac{\partial \mathbf{E}}{\partial t} \quad (2.4)$$

Here, ρ is the electric charge density and μ_0 and ε_0 denote magnetic permeability and electric permittivity of free space. The relative permittivity being denoted by ε_r , the analysis of photonic structures in terms of electric field is governed by the

Maxwell's wave equation expressed as:

$$\frac{\partial^2 \mathbf{E}}{\partial x^2} + \frac{\partial^2 \mathbf{E}}{\partial y^2} + \frac{\partial^2 \mathbf{E}}{\partial z^2} - \varepsilon_0 \varepsilon_r \mu_0 \frac{\partial^2 \mathbf{E}}{\partial t^2} = 0. \quad (2.5)$$

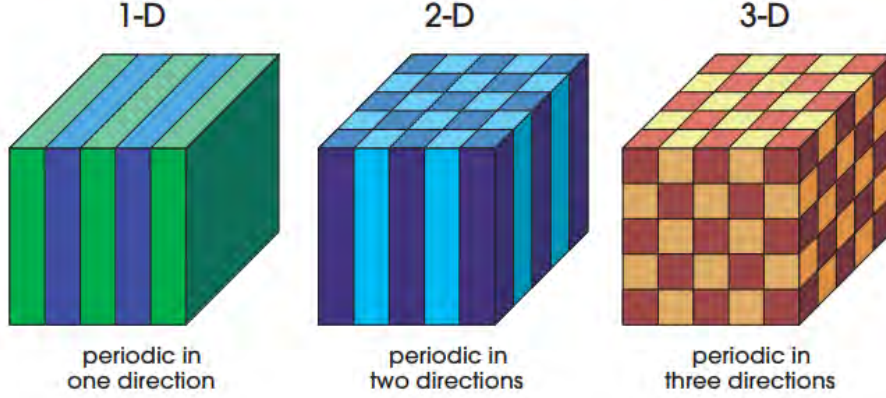


Figure 2.1: Schematics of 1D, 2D and 3D photonic crystals [3].

2.2 Photonic Crystals

Photonic crystals are a special type of structures, consisting of periodic modulation of dielectric constants of the constituent materials, which can modify the behavior of light along the direction of periodicity. Based on the periodicity of the structure, photonic crystals can be classified into three categories. When the periodicity is maintained along a single axis and the structure remained homogeneous along the other two axes, it is termed as 1D photonic crystal. Likewise, maintaining periodicity along two of the axes keeping the homogeneity along the third results in a 2D photonic crystal and periodic modulation of refractive index along all three axes results in a 3D photonic crystal. Schematic representation of 1D, 2D, and 3D photonic crystals are shown in Fig. 2.1.

2.3 2D Photonic Crystals

As our studied periodic structure is identical to a 2D photonic crystal with square lattice of dielectric columns, the E-k band structure and photonic bandgap in such crystal will be explained in detail in this section. A representative of such 2D PC is

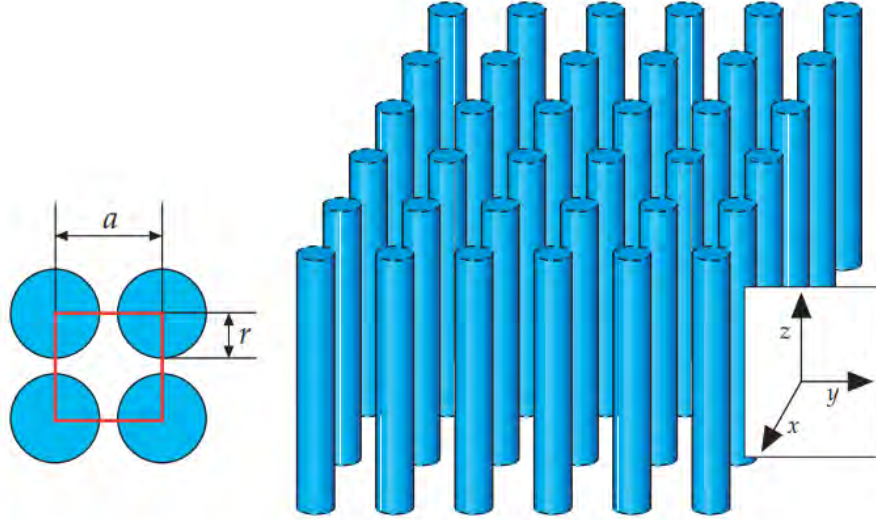


Figure 2.2: A schematic representation of 2D photonic crystal consisted of dielectric columns suspended in air. The square shape unit cell is also shown where lattice constant is denoted by a and radius of the nanowires is denoted by r [3].

shown in Fig. 2.2 (square shape unit cell is also shown), where the periodic variation of air and dielectric cylinders along the x and y directions are maintained. For this square shape array, the Brillouin zone in the reciprocal lattice is also a square shape area, where the irreducible Brillouin zone is a triangle consisting of one-eighth of the square region. The high symmetric k -points at the corners of the irreducible Brillouin zone are denoted as Γ , X , and M respectively for (000) , (100) , and (110) directions in the reciprocal lattice.

2.3.1 Photonic band structure

When light propagation in the xy plane is considered, the behavior of light differs significantly depending on the polarization of light. As we know that transverse electric (TE) polarized light have in-plane electric field ($\mathbf{E}(\rho).z = 0$) perpendicular to the direction of propagation and out-of-plane magnetic field perpendicular to both the electric field and the propagation direction. On the contrary, transverse magnetic (TM) polarized light's electric field is normal to the plane and magnetic field is in-plane. Both TE and TM band structures of this array for a change in momentum along the irreducible Brillouin zone (Γ - X - M - Γ) is shown in Fig. 2.3.

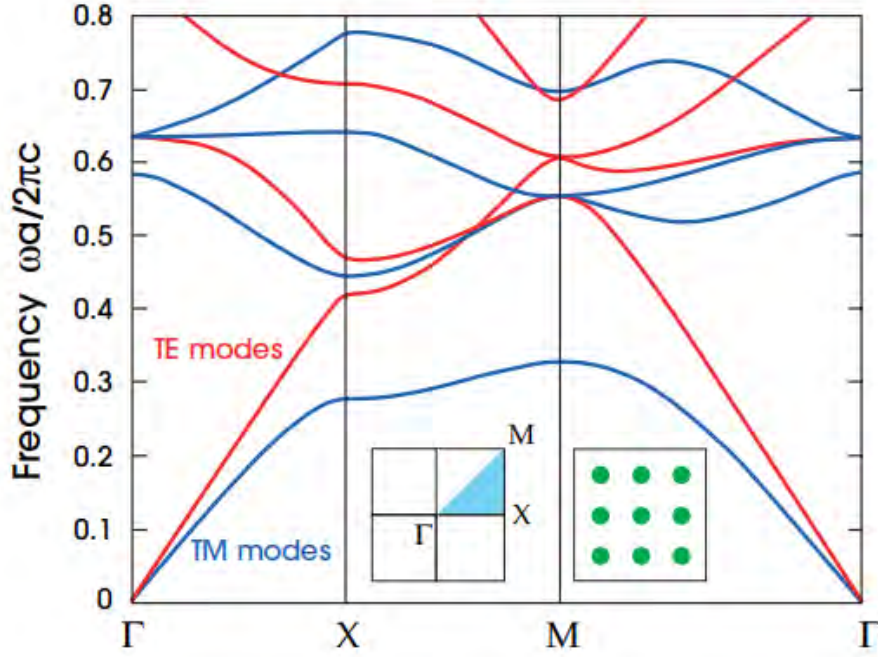


Figure 2.3: The photonic bandstructure of a 2D PC consisted of square shape unit cell of dielectric cylinders suspended in air. The unit cell and the Brillouin zone are shown in the inset. The irreducible Brillouin zone is marked with the blue triangle [3].

2.3.2 Photonic bandgap

As can be seen from the TM band structure, there appears a particular band of frequency where no frequency band is permitted. In other words, light of this particular frequency band is not permitted to propagate through the structure along the direction of propagation. This band of frequency is termed as photonic band gap (PBG) of the photonic crystals.

2.3.3 Origin of photonic bandgap

The origin of this PBG is better understood with the help of field distributions. The displacement fields at the high symmetric X and M points for band1 and band2 are depicted in Fig. 2.4. Band1's frequency being lower, E-field energy of a mode with this frequency is mostly concentrated in the dielectric columns (as these are of high-epsilon compared to air). But, for upper bands need to be orthogonal to the lower ones, a nodal plane appears in the dielectric regions for a mode with a frequency from band2. As a result, E-field of energy of a high frequency mode of band2 becomes concentrated in the low-epsilon air region. Because of this

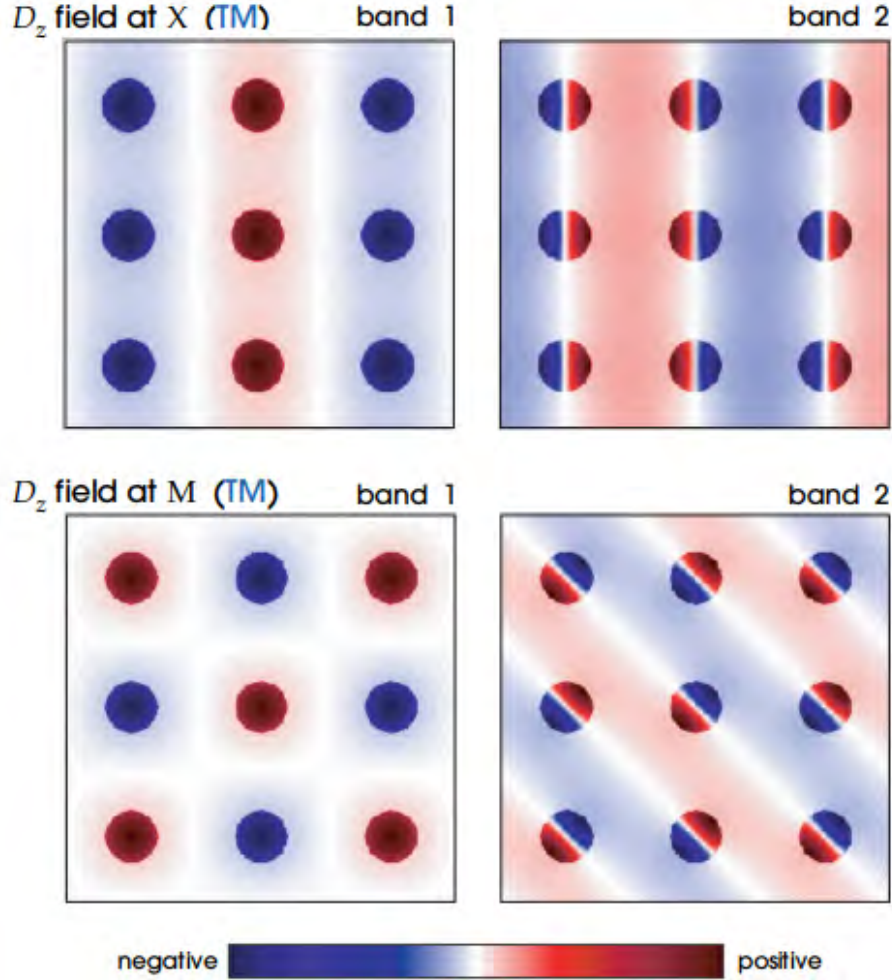


Figure 2.4: Displacement field distributions at high symmetric X and M points of the irreducible Brillouin zone for TM polarization [3].

significance difference in E-field energy concentration in the dielectric, a photonic bandgap appears. As E-field is along the dielectric axis for TM polarized light, large concentration of E-field energy in the high-epsilon region is possible. But, for the E-field being in-plane in case of TE polarized mode, the possibility of large concentration factor is reduced by the forcing of E-field energy out of the dielectric columns. As a result, PBG appears for TM mode only and no gap is found for TE modes.

2.4 Light Scattering

Light scattering can be defined as the redirection of light that occurs when an electromagnetic wave (EM) comes into contact with a scattering object. When

the EM wave interacts with the scattering particle, the electron orbits inside the particle's constituent molecules are disrupted at the same frequency as the incoming wave's electric field. The periodic separation of charge within the molecule caused by the disturbance of the electron cloud is known as an induced dipole moment. The fluctuating induced dipole moment acts as a source of electromagnetic radiation, resulting in dispersed light. As the scattered light are generally at the same frequency as the incident light, this phenomenon is termed as elastic scattering. A schematic of this elastic scattering is represented in Fig. 2.5. In our case, each dielectric column can be considered as an individual scatterer of light. Hence, a brief overview of the involved scattering processes will enhance the understanding of the propagation of light through dielectric arrays.

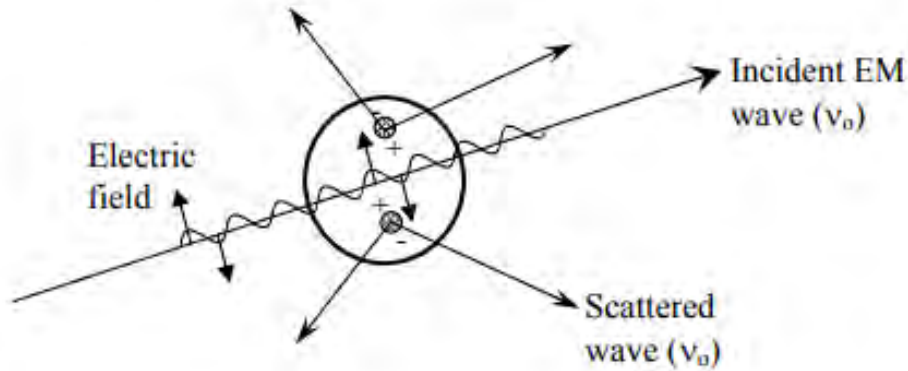


Figure 2.5: Elastic scattering of light by a particle [4].

2.4.1 Rayleigh Scattering

When light or other electromagnetic radiation is scattered primarily by the particles that are considerably smaller than the wavelength of the radiation, this phenomenon is known as Rayleigh scattering. Specifically, the electric polarizability of the scattering particles causes Rayleigh scattering. The charges inside a particle are affected by the oscillating electric field of a light wave, which makes them travel with the same frequency. As a result, the particle transforms into a tiny radiating dipole, and we observe its radiation as scattered light. As Rayleigh scattering depends on the relative size of the scatterer, the criteria for Rayleigh scattering

can be formulated from the following dimensionless parameter [4]:

$$\alpha = \frac{2\pi r}{\lambda}. \quad (2.6)$$

Here, r is the radius of the scattering particle and λ denotes relative scattering wavelength. When the condition $\alpha \ll 1$ is satisfied, Rayleigh scattering is said to be the dominant process involved. As α varies from 0.31 to 1.41 for our considered diameters (60 nm to 90 nm) and wavelengths (250 nm to 600 nm), Rayleigh scattering is not considered in the analysis. But, for Mie scattering (to be discussed later) the criteria on particle size is relaxed. Fig. 2.6 represents a comparison of Rayleigh and Mie scattering depending on particle size.

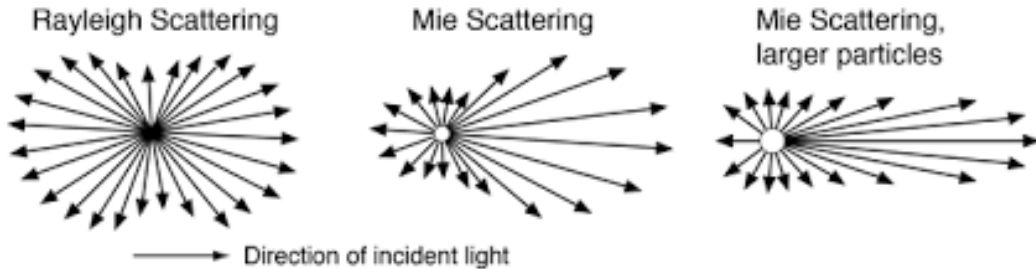


Figure 2.6: Rayleigh scattering and Mie scattering [5].

2.4.2 Bragg scattering

Bragg scattering is generally attributed to the collective scattering of light from a periodic structure. Long range periodicity is a must for this scattering effect to be dominant. In other words, Bragg scattering can be elucidated as the process where multiple reflection of light from the interface of the constituent dielectrics either interfere constructively or destructively depending on the structural parameters. This phenomenon of constructive and destructive interference is depicted in Fig. 2.7. In this process, the crystal structure is modelled as a collection of discrete parallel planes divided by a constant parameter d . When the reflected waves off the multiple planes interfere constructively, Bragg peaks are produced in the reflectance spectra. This constructive interference results in when a phase shift of 2π is maintained between the reflected waves. Alternatively, this phenomenon of constructive interference of reflected waves can be considered as the creation of a

gap in the transmittance spectra, which may also be termed as photonic bandgap.

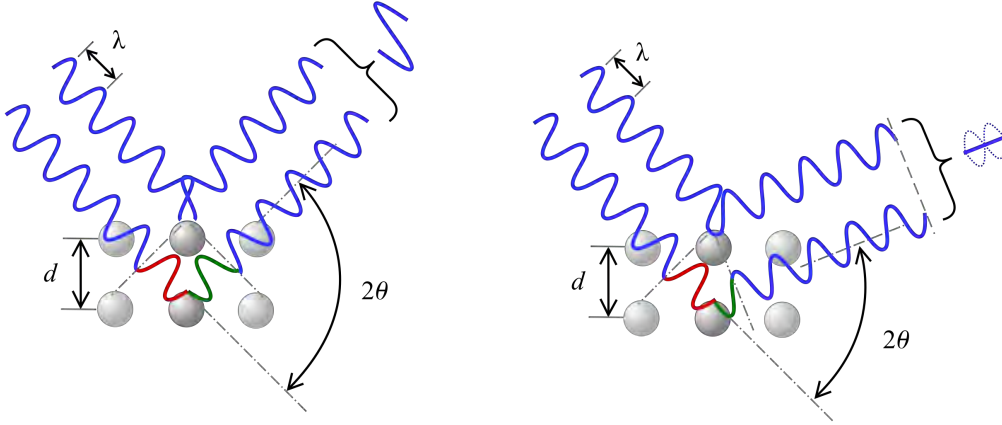


Figure 2.7: Constructive and destructive interference due to Bragg process in a crystal [6].

2.4.3 Mie scattering

Mie scattering is the elastic scattering of EM wave by particles with a diameter that is comparable to the wavelength of the incident wave. Schematic of Mie scattering depending on particle size is represented in Fig. 2.6. As $\alpha \approx 1$ according to the formulation of Eq. 2.6 in our study, Mie process is expected to be dominant in our analysis. The interaction of the EM radiation of light with that of the scattering particle (generated at the particle's surface due to the presence of electron) may result in a diffraction pattern similar to the case of Bragg diffraction. However, contrary to Bragg process, long range periodicity is not necessary for the Mie process. The scattering of light by an individual scatterer irrespective of the arrangement of its adjacent atoms is generally termed as Mie scattering. The coupling of the modes of a particular scatterer with its adjacent one results in Mie resonance. Due to this coupling, photonic bandgap may appear even in aperiodic structures [41].

Chapter 3

Analyzed Structures and Computational Methods

The structural designs considered in our study and the computational methods involved in the analysis will be discussed in this chapter. To have an understanding of the effects of randomness on light transmission, periodic, correlated random, and uniform random systems are considered. Finite difference time domain (FDTD) analysis technique is used as the computational method. The details of the simulation setup and methodology will be discussed here.

3.1 Self-organized Growth of Nanowire Array

As the diameters and random patterns in our study are considered according to experimentally reported dimensions of self-organized nanowire array, self-organized growth process of such nanowire arrays is discussed in brief in this section. On the (001) Si substrate, under nitrogen-rich conditions, and without the use of any foreign- or Ga self-catalyst, self-organized GaN-nanowire arrays can be grown using plasma assisted molecular beam epitaxy (MBE). As Si-N bonding is more energetically favourable than Ga-N bonding at the early stages of the growth process, a layer of Si_xN_y is formed in between the Si substrate and GaN nanowire [57–60]. This Si_xN_y layer initiate the nanowire formation process by making it easier for the Ga atoms to be incorporated onto the growth plane. It is noteworthy that these nanowires form spontaneously on the growing substrate and a random pattern

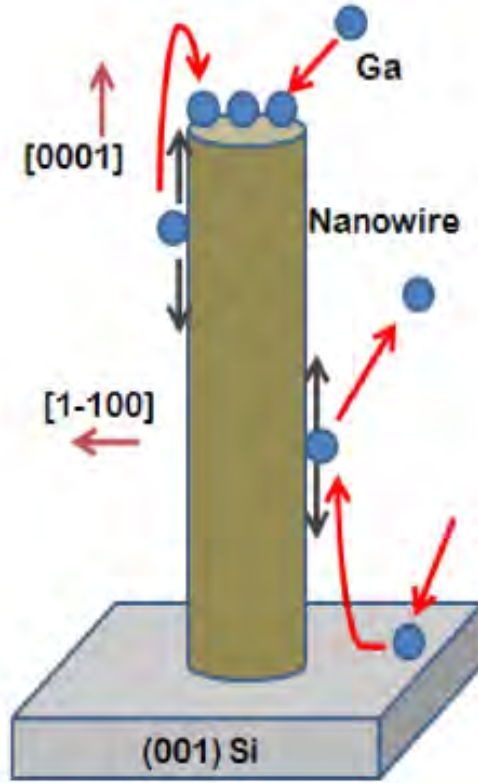


Figure 3.1: Growth process of GaN nanowire on Si substrate [7].

is generated. The growth mechanism is illustrated in Fig. 3.1. As can be seen from the figure, adatoms impinging on the Si substrate diffuses towards the sidewall of the nanowire by overcoming the energy barrier between Si and GaN. However, these adatoms may not contribute to the growth process by being desorbed from the sidewall. Again, adatoms impinging on the upper sidewall are attracted by the low potential of the top surface. As a result, adatoms impinging around the top surface majorly contribute to the nanowire growth. SEM images of nanowire arrays grown employing this MBE technique are shown in Fig. 3.2, where the effects of Ga fluxes on the growth of nanowire array is evident. In this way, controlling the growth parameters, the diameters of the nanowires can be varied from 25 nm to 200 nm [61].

Again, SEM image of the top view of such MBE grown self-organized nanowire array is shown in Fig. 3.3(a), which was grown with a Ga flux of 1.65×10^{-7} Torr at 800°C temperature [9]. Applying image processing on this image, the pattern of Fig. 3.3(b) is generated. Circular approximation is used to simplify the pattern generation. Mimicking this pattern of self-organized nanowire array, random

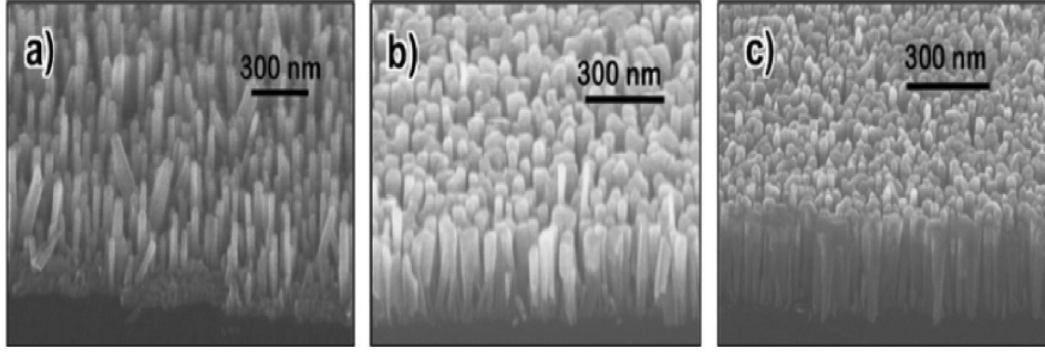


Figure 3.2: SEM images of GaN nanowires grown with Ga fluxes of (a) 3×10^{-8} , (b) 7.8×10^{-8} , and (c) 9×10^{-8} Torr [8].

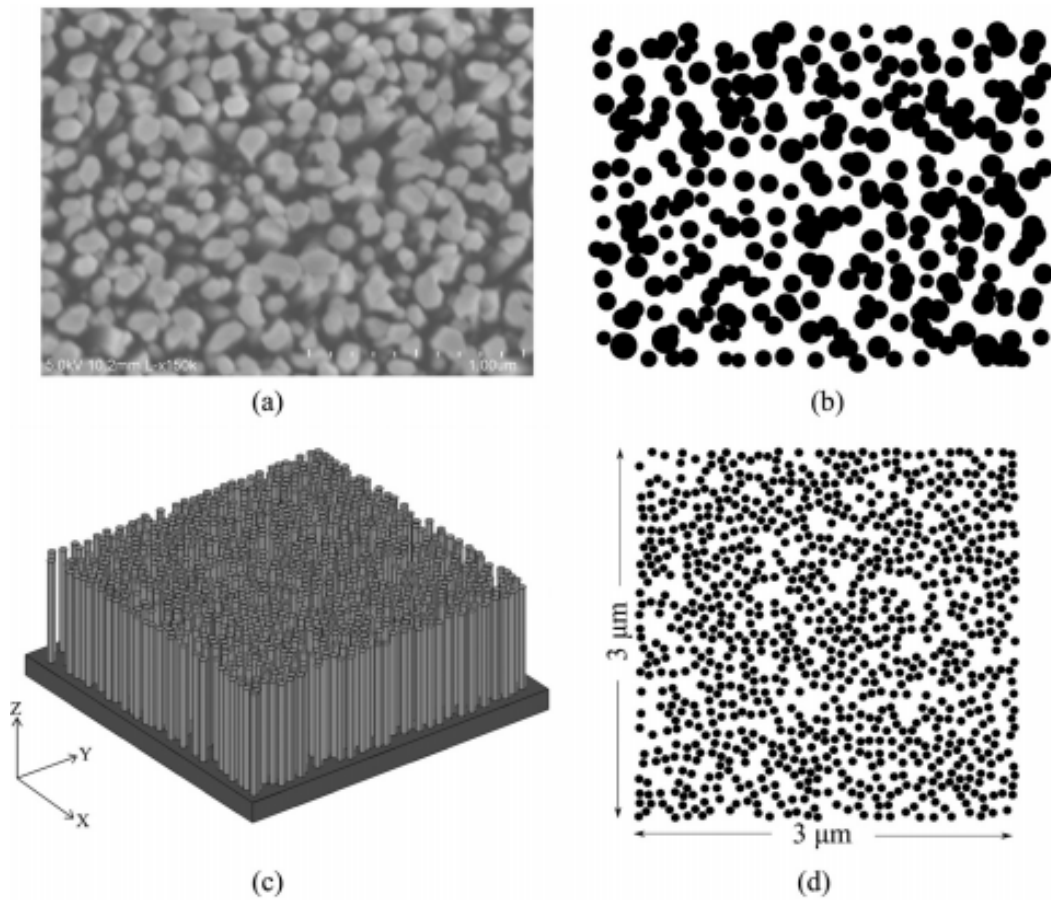


Figure 3.3: (a) SEM image of the top view of MBE grown self-organized GaN nanowires on Si; (b) transferred pattern generated through image processing; (c) A 3D schematic diagram of GaN nanowire array and (d) corresponding 2D cross-section in the x-y plane [9].

arrays in our study are generated with identical dimensions and areal densities. 3D schematic diagram and 2D cross-section of a random nanowire array similar to that considered in our analysis are shown in Figs. 3.3(c) and 3.3(d) respectively.

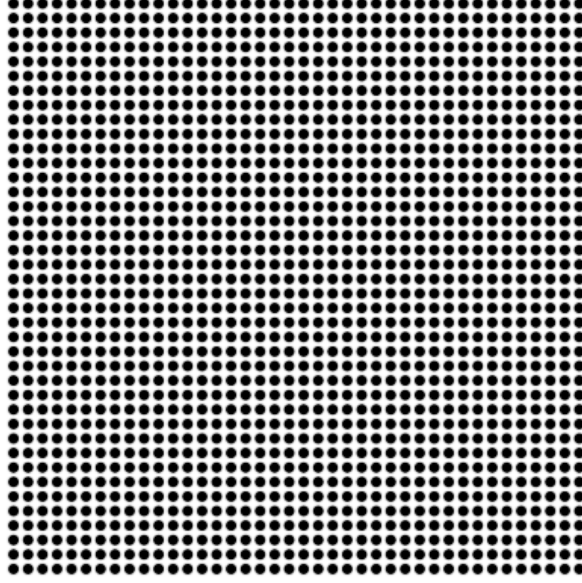


Figure 3.4: Cross-sectional view of a $3 \times 3 \mu\text{m}^2$ periodic array with 50 % ff having identical nanowires of 60 nm diameter.

3.2 Device Structure

Four types of structures – periodic, correlated weakly disordered, correlated strongly disordered, and uncorrelated disordered - are considered in this study.

3.2.1 Periodic nanowire array

GaN nanowires (NWs) suspended in air in a square shape lattice arrangement constitute the periodic array in our study. NWs are vertically aligned along the z axis and periodicity is maintained along the x and y directions. A schematic of the periodic array with 60 nm diameter and 50% fill-factor in the xy cross-sectional plane is shown in Fig. 3.4. Keeping the total system area fixed at $3 \times 3 \mu\text{m}^2$, diameters and fill-factors are varied from 60 – 90 nm and 30 – 50% respectively. Here, fill-factor (ff) is calculated as

$$\text{ff} = \frac{\frac{1}{4}\pi d^2}{a^2}, \quad (3.1)$$

where d denotes the diameter of the nanowires and a is the lattice constant.

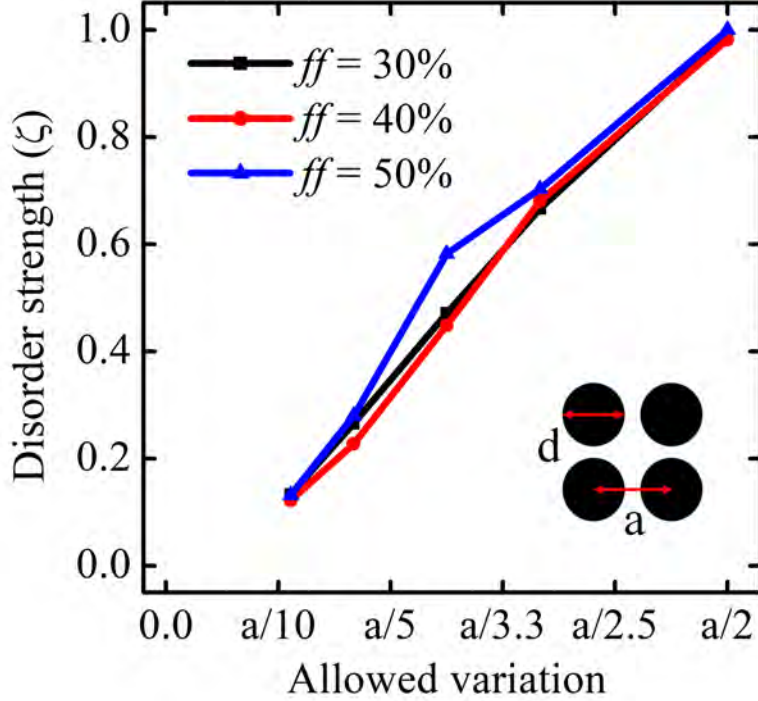


Figure 3.5: Maximum achievable disorder strength (ζ) for different allowed variation. Square shape unit cell of the periodic array is shown in the inset.

3.2.2 Correlated random array

Correlated disordered structures are generated from the periodic array with identical diameters and fill-factors. P ($P \in [0, 100]$) being the percentage randomness parameter, new coordinates $(x + dx, y + dy)$ for the correlated array was generated from the NW co-ordinates (x, y) of the periodic array based on the following equations:

$$\begin{aligned} dx &= (P/100) \times r_x \times R \\ dy &= (P/100) \times r_y \times R \end{aligned} \quad (3.2)$$

Here, $\{r_x, r_y\}$ are random numbers generated uniformly within the range $[-1, 1]$ and R denotes the allowed variation. For avoiding the overlapping of nanowires, a newly generated coordinate is taken only if the center to center distances from the nanowire to its adjacent are greater than the diameter. Otherwise this coordinate is discarded and a new one is generated and compared.

To quantitatively measure the degree of randomness in such structures, disorder

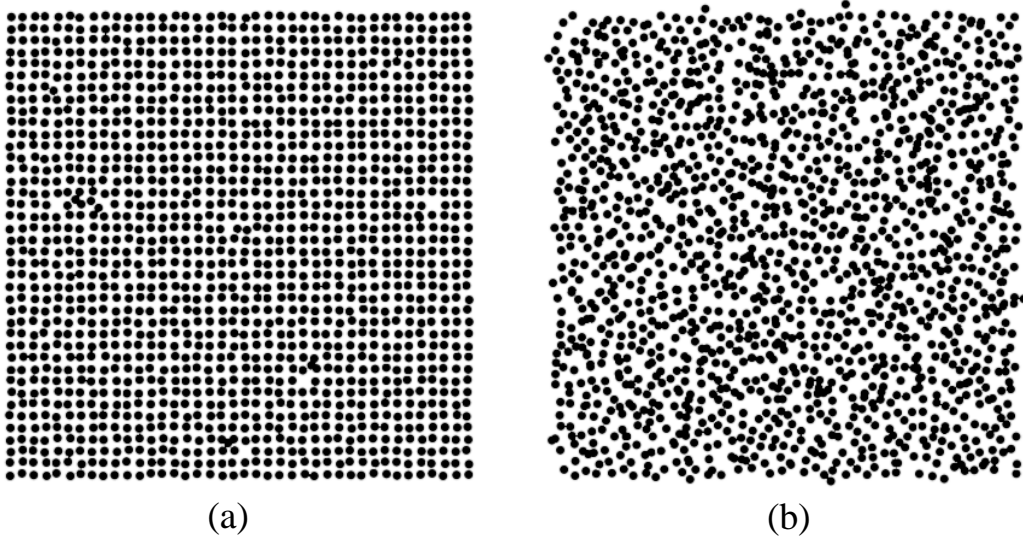


Figure 3.6: Cross-sectional views of (a) correlated weakly disordered ($\zeta = 0.1425$) and (b) correlated strongly disordered ($\zeta = 0.9963$) arrays with 50 % ff having identical nanowires of 60 nm diameter.

strength (ζ) is calculated using the following relation:

$$\zeta = 1 - \frac{1}{N-1} \sum_{j=1}^N \left(\frac{A_j - \mu_A}{\sigma_A} \right) \left(\frac{B_j - \mu_B}{\sigma_B} \right) \quad (3.3)$$

Here, A and B are 1D vectors containing the refractive index profile of the periodic and random arrays respectively. N denotes total number of elements in the vector and μ and σ are the mean and standard deviation of the corresponding vectors. The relation of this disorder strength with allowed variation is shown in Fig. 3.5 for different fill-factors of the array. As can be seen, restricting allowed variation limits the randomness in the weakly disordered regime even with the highest value (100 %) of percentage randomness parameter. So, in our analysis, allowed variation is set to $a/2$ for getting a disorder strength of almost unity. Two configurations of disordered structures of 60 nm diameter and 50 % fill factor with 25 % ($\zeta = 0.1425$) and 100 % ($\zeta = 0.9963$) randomness are represented in Figs. 3.6(a) and 3.6(b) respectively.

3.2.3 Uniform random array

For getting uniformly random structures, we have generated random numbers using uniform random distribution to select the x and y coordinates of the centers

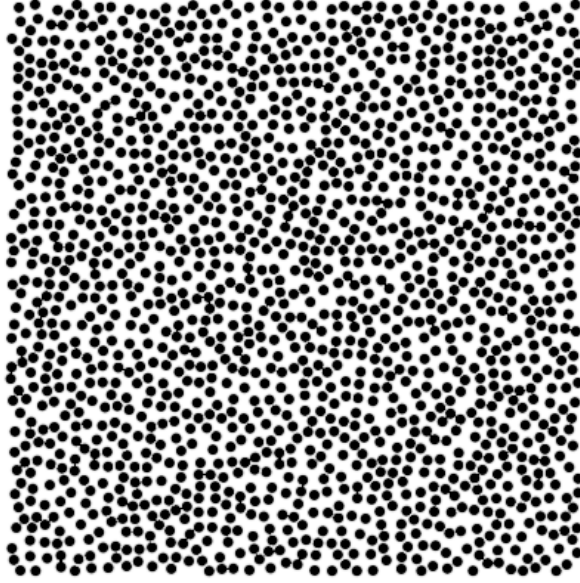


Figure 3.7: Cross-sectional view of a $3 \times 3 \mu\text{m}^2$ uniform random array with 50 % ff having identical nanowires of 60 nm diameter.

of the GaN nanowires. Desired fill factor for the random structure is ensured by calculating the total area needed to be covered by the nanowires and then the number of nanowires hence the number of random coordinates are determined. The coordinates are placed in the range $\{Sx, Sy\} \in [-1.5, 1.5]$ in such a way that center to center distance of adjacent nanowires are greater than the diameter in order to avoid overlapping. Here, Sx and Sy indicate the overall dimension of the structure along x and y directions respectively. The cross-sectional view of a uniformly generated random array with 60 nm diameter and 50 % fill-factor is shown in Fig. 3.7.

3.3 Photonic Band-structure of Periodic Array

The band structures of the periodic array is determined by using the MPB package [62]. MPB (MIT Photonic Bands), an open source eigen frequency solver, computes the band structures of periodic arrays by calculating the eigenstates of Maxwell's equations. Only a unit cell, defining the high symmetric Γ , X, and M points of the irreducible Brillouin zone (marked with a blue triangle in the inset of Fig. 3.8), is needed to be simulated to get the whole band structure. The lower eight frequency bands, starting from the fundamental, are considered to look out for the photonic band gap (PBG) in our desired frequency range. The TE (red) and

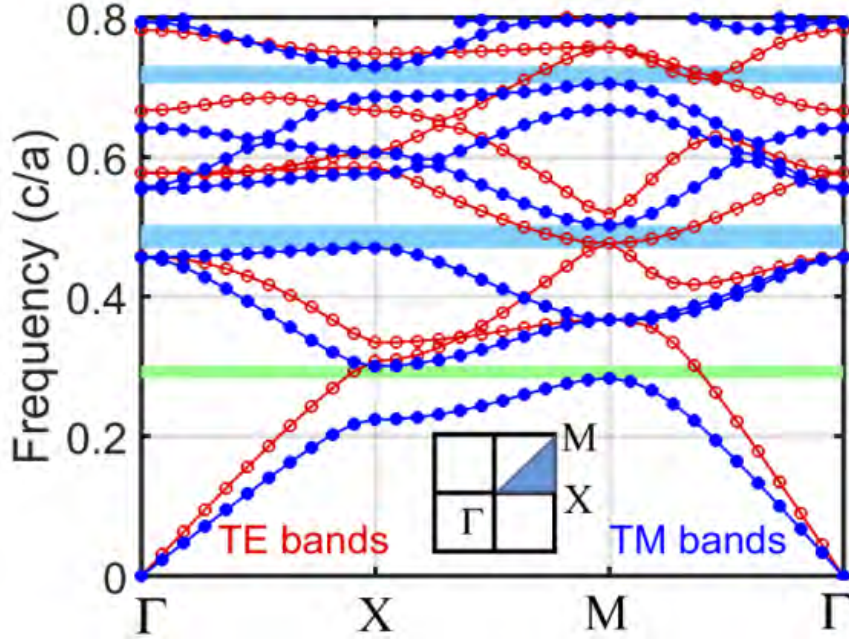


Figure 3.8: TE and TM Band structures of the periodic NW array. The irreducible Brillouin zone for the square shape unit cell is marked with a blue triangle in the inset.

TM (blue) band structures of our analyzed periodic GaN NW array is presented in Fig. 3.8, which confirms the existence of TM bandgap.

3.4 Finite Difference Time Domain Analysis

Finite Difference Time Domain (FDTD) analysis involves the numerical solving of Maxwell's equations by dividing the total computational space in a discrete grid.

3.4.1 Simulation details

Open source software package MEEP (MIT Electromagnetic Equation Propagation) is used as the FDTD analysis tool to study the transmission characteristics of both periodic and disordered structures in our study [63]. MEEP divides the 3D computational space into cubic grids and computes the \mathbf{E} and \mathbf{H} field components at different locations of the cubes. Such discrete cubes are termed as Yee lattice, a representation of which is shown in Fig. 3.9. The E_x , E_y , and E_z components of the \mathbf{E} field are stored at the cube edges, while the H_x , H_y , and H_z components of the \mathbf{H} field are stored at the faces of the cube.

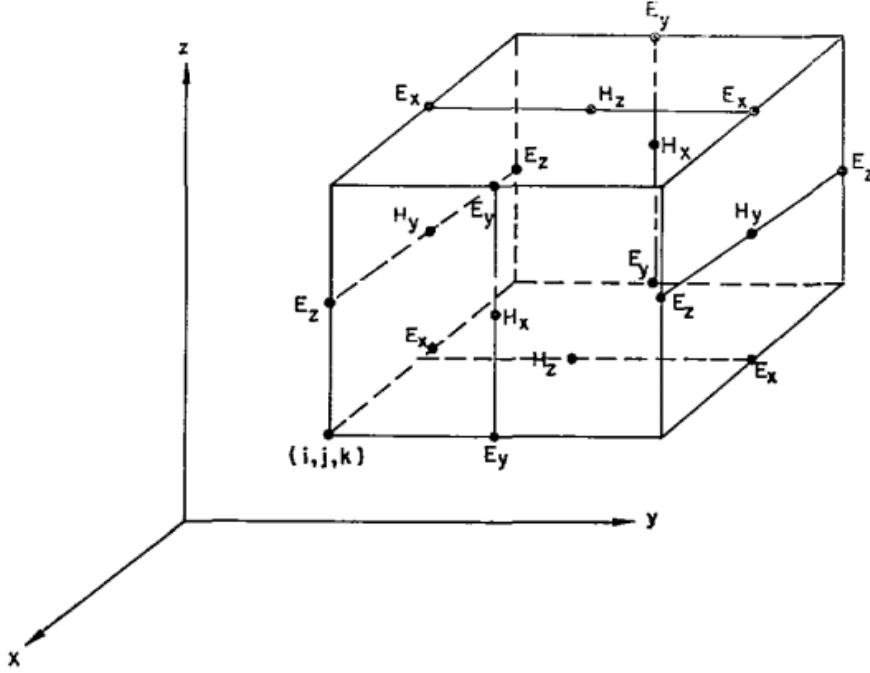


Figure 3.9: Yee lattice in a 3D computational space [10].

FDTD technique is particularly convenient for calculating the flux spectrum over a broad wavelength range in a single simulation. By obtaining the Fourier-transform of the response of the computational region to a short pulse, transmittance and reflectance spectra for broadband wavelength can be easily calculated. A power monitor is needed to be placed at the desired location where the flow of power is to be recorded. The transmitted power through this monitor is then calculated by integrating the poynting vector as follows,

$$P(\omega) = \text{Re}\{\hat{\mathbf{n}} \cdot \int \mathbf{E}_\omega(\mathbf{x})^* \times \mathbf{H}_\omega(\mathbf{x}) d^2\mathbf{x}\} \quad (3.4)$$

Here, $\hat{\mathbf{n}}$ is the direction normal to the monitor. Fourier-transformed fields, $\mathbf{E}_\omega(\mathbf{x})$ and $\mathbf{H}_\omega(\mathbf{x})$ are stored at each location of the monitor for each time steps. Then, $P(\omega)$ is obtained by accumulating the results of the discrete time steps.

For calculating the reflectance spectra, two simulation is needed - one without the scatterer and one with the scatterer. The monitor is placed at the same location for both the simulations. This is due to the fact that incident flux is needed to be subtracted to get only the reflected flux from the scatterer. If Fourier-transformed fields without the scatterer are $\mathbf{E}_\omega^{(0)}(\mathbf{x})$ and $\mathbf{H}_\omega^{(0)}(\mathbf{x})$ and those with the scatterer are

$\mathbf{E}_\omega(\mathbf{x})$ and $\mathbf{H}_\omega(\mathbf{x})$, then the reflected power can be expressed as

$$P_r(\omega) = \text{Re}\{\hat{\mathbf{n}} \cdot \int [\mathbf{E}_\omega(\mathbf{x}) - \mathbf{E}_\omega^{(0)}(\mathbf{x})]^* \times [\mathbf{H}_\omega(\mathbf{x}) - \mathbf{H}_\omega^{(0)}(\mathbf{x})] d^2\mathbf{x}\} \quad (3.5)$$

Both reflected and transmitted power are normalized with the incident power to get the reflectance (R) and transmitted (T) spectra.

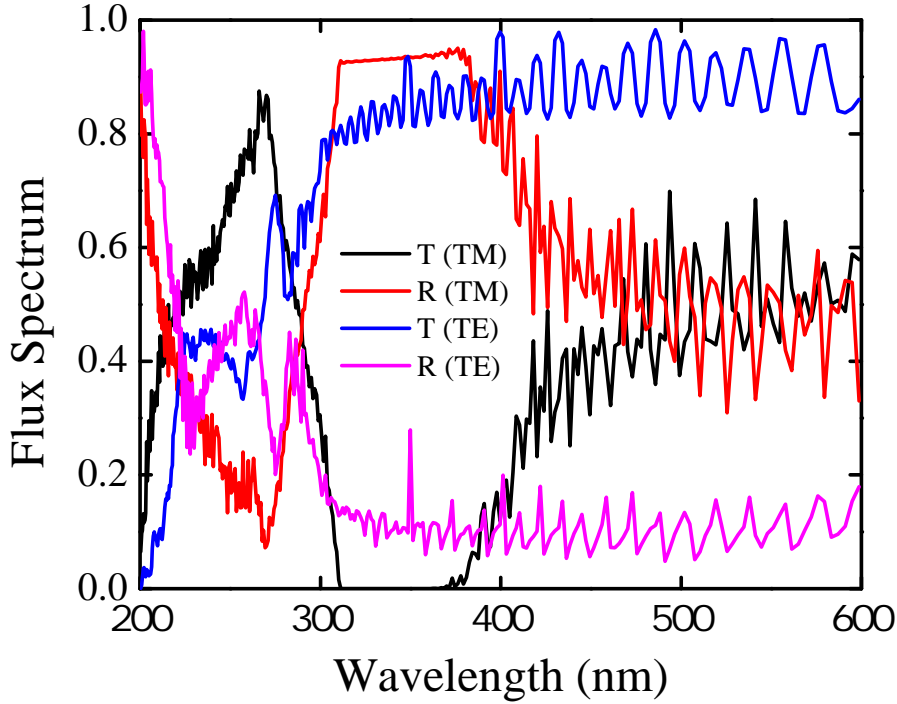


Figure 3.10: Transmittance (T) and reflectance (R) spectra of periodic GaN nanowire array with 70 nm diameter and 50 % ff for both TE and TM modes.

3.4.2 Benchmarking with band-structure

To calculate the flux spectra in our study, a gaussian pulse source with wavelength ranging from 200 nm to 600 nm is placed at the left of the array. A reflectance monitor is placed in the air region between the source and starting plane of the array and a transmittance monitor is placed at the right of the array to measure the reflectance (R) and transmittance (T) spectra respectively. Perfectly matched layer (PML) layer boundary condition is used with the PML thickness chosen to be greater than the highest wavelength of the source to absorb the light out of the computational region. For a periodic array of GaN with 70 nm diameter

and 50 % ff, the recorded reflectance and transmittance spectra for both TE and TM modes are plotted as a function of wavelength in Fig. 3.10. It can be depicted here that, transmittance is almost zero in the wavelength range of 310 nm to 372 nm, which indicates the existence of PBG like transmission gap for TM mode. For a periodic array with similar diameter and fill-factor, a TM PBG at around 315 nm is also evident from the dispersion relation of Fig. 3.8 (marked with green region), which confirms the direct correlation of the PBG to the transmission gap of the periodic systems. As such transmission gap is absent for TE modes in our considered wavelength region for the considered dimensions of the GaN nanowire, the transmission characteristics of TM polarized light will be focused in this study.

3.5 Inverse Design-based Optimization

Electromagnetic simulation usually generates electric field distribution for a given permittivity distribution according to the Maxwell's equation as follows:

$$\mathbf{E} = \left(\left(\nabla \times \frac{1}{\mu} \nabla \times \right) - \omega^2 \epsilon \right)^{-1} (-i\omega \mathbf{J}) \quad (3.6)$$

Here, current density \mathbf{J} represents input mode source of frequency ω . \mathbf{E} denotes electric field and μ and ϵ are magnetic permeability and electric permittivity respectively. In this process, the efficiency of the device depends on the intuition of the designer and the design flexibility is also limited. In this regard, inverse design technique has been proved to be an efficient method to get user-specified output with customized designs.

3.5.1 Algorithm

Let us consider an output mode j is specified by the user for an input mode i in an inverse design problem which is to be bounded between a specified limit. Output electric field ϵ_{ij} is to be recorded in the output port over a surface S_{ij} . Then inverse design technique will generate an optimized structure that satisfy both

$$\nabla \times \mu_0^{-1} \nabla \times \mathbf{E}_i - \omega_i^2 \epsilon \mathbf{E}_i = -i\omega_i \mathbf{J}_i \quad (3.7)$$

and

$$\alpha_{ij} \leq \left| \iint_{S_{ij}} \boldsymbol{\mathcal{E}}_{ij}^* \cdot \mathbf{E}_i \, dS \right| \leq \beta_{ij} \quad (3.8)$$

Here, the modal overlap of the input electric field with the specified output mode electric field is to be bounded between the limit α_{ij} to β_{ij} . The full inverse design process can be divided into the following steps:

3.5.2 Initial structure

An initial structure is needed to be defined based on which the optimized structure is generated by changing the permittivity of the design area within the specified limit. In our case, periodic and random nanowire arrays are considered as the initial structures as shown in Figs. 3.11 and 3.12 respectively. Design region is marked with red dotted region. Source is injected along left port marked as “3” and output is recorded along right ports where the top port is marked as “1” and the bottom one is marked as “2” in the figure.

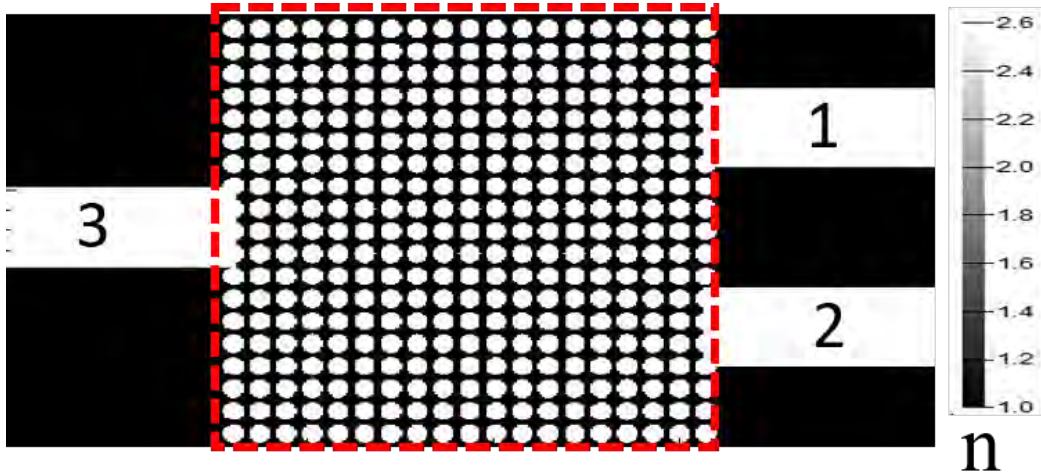


Figure 3.11: Periodic nanowire array initial structure. Design region is marked with red dotted region. Source is injected along left port marked as “3” and output is recorded along right ports marked as “1” and “2”.

3.5.3 Optimization

SPINS-B have been employed for running the optimization in our work. SPINS-B is the open source version of SPINS (Stanford Photonics Inverse Design Software) [64]. Gradient based optimization is used here. The basic steps of optimization in

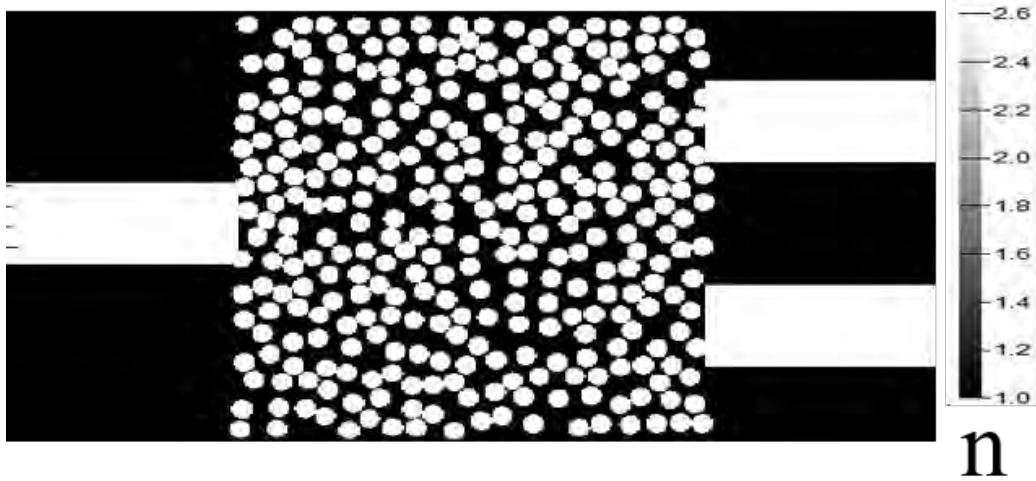


Figure 3.12: Random nanowire array initial structure.

SPINS is depicted in the flowchart of Fig. 3.13. In this method, after setting up the simulation domain, a figure of merit or objective function is needed to be defined. Spins computes the gradient of the objective function and tries to minimize it by moving in the opposite direction of the gradient. So the objective function should be formulated according to the specification of the user. In case of our study on power splitter, the objective is to maximize the power transfer to the output ports. As spins minimizes the objective function, the objective function can be expressed as

$$f_{obj,i} = 1 - |C_{i,3}E|^2; \quad i = 1, 2 \quad (3.9)$$

Here, $|C_{i,3}E|$ denotes the modal overlap of electric field E with the target mode C . The summation of these two objective functions consists the final objective as follows:

$$f_{obj} = f_{obj,1} + f_{obj,2} \quad (3.10)$$

For wavelength demultiplexers, the target is to maximize the power transfer at a particular wavelength to a specific port, while minimizing the power transfer of the same wavelength at the other output port. To transfer 650 nm wavelength along port1 and 550 nm wavelength along port2, the objective function can be expressed as

$$\begin{aligned} f_{obj,1} &= 1 - |C_{1,3}^{650} E|^2 + |C_{2,3}^{650} E|^2 \\ f_{obj,2} &= 1 - |C_{2,3}^{550} E|^2 + |C_{1,3}^{550} E|^2 \end{aligned} \quad (3.11)$$

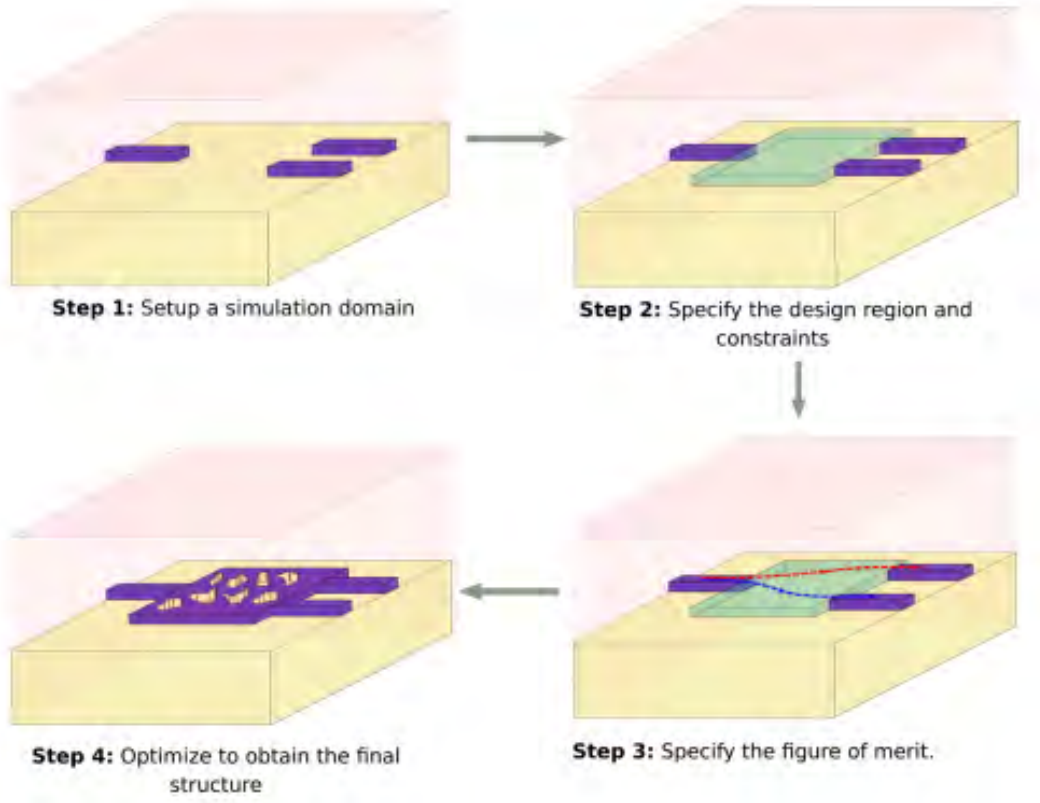


Figure 3.13: Flow chart of the steps to be followed to design a photonic device using inverse design technique [11].

Here, $|C_{i,3}^{650} E|$ denotes the modal overlap of the electric field at 650 nm wavelength with the target mode C_i of the output port i . The final objective is the summation of these two sub-objectives in this case also.

3.5.4 Discretization

During optimization the permittivity of the design region is allowed to vary continuously within the specified limit. But, to ensure the realizability of the device, the optimized structure is discretized by using binary discretization technique. In our study, a threshold permittivity (ϵ_{th}) is chosen as

$$\epsilon_{th} = \text{Average}(\epsilon_{air}, \epsilon_{GaN}). \quad (3.12)$$

Here, ε_{air} and ε_{GaN} denotes the permittivity of air and GaN NW respectively. Then the discretized structure is generated based on the following condition:

$$\begin{aligned} &\text{If } \varepsilon > \varepsilon_{th}; \text{ then } \varepsilon = \varepsilon_{GaN} \\ &\text{else } \varepsilon = \varepsilon_{air} \end{aligned} \tag{3.13}$$

3.5.5 FDTD simulation

FDTD simulation is employed on the discretized structure to generate the transmission spectra over a broad wavelength region. Field distributions at specific wavelengths are also observed to ensure that the performance objective is fulfilled properly. For running the FDTD simulations, we have used Lumerical FDTD as the analysis tool. Higher order mesh is employed in the GaN regions to define the structures properly at the coarse boundary. By injecting a mode source from the left port of the device, output is recorded at the right ports.

Chapter 4

Results and Discussion

Results of our study are demonstrated with associated figures in this section and the corresponding analysis and explanation of the results are also carried out. First of all, the light transmission characteristics in both periodic and random arrays is discussed in detail. The origin of transmission gap in random arrays and the tuning of the gap are also demonstrated. The later part of this chapter shows the potential application of such systems in designing power splitters and wavelength demultiplexers based on inverse design technique.

4.1 Light Transmission Characteristics

4.1.1 Origin of transmission gap

To understand the behavior of light transmission through disordered dielectric arrays, correlated randomness is introduced gradually in the periodic structure and the corresponding change in the transmittance spectra is observed. For our representative periodic array with 50% ff and 60 nm diameter, the appearance of transmission gap (from 268 nm to 320 nm) is evident in the transmittance spectra as shown in Fig. 4.1. In the passband region, some spikes are also evident. These spikes arises due to Fabry-Perot (FP) resonance between the boundaries of the nanowire array and the spike-to-spike distance follows the equation:

$$\Delta\lambda_m = \frac{2L}{m} - \frac{2L}{m+1} \quad (4.1)$$

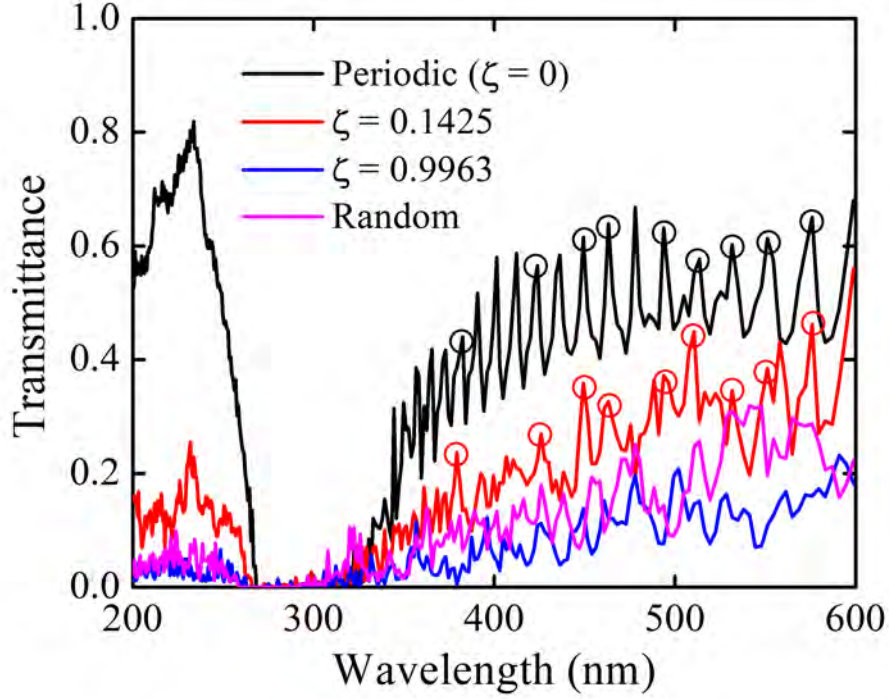


Figure 4.1: Transmittance spectra for periodic, correlated disordered, and uniform random systems with 50 % ff and 60 nm diameter.

Here, L denotes system length (distance between the boundaries) and m is the mode number of FP resonance.

Now, introducing randomness in correlation with the periodic structure results in a transmission gap in almost at the same wavelength region as the periodic one. Though a shrinkage in the gap occurs for the disordered arrays, the sustainability of the gap even at the highest value of disorder strength is quite interesting. It is also noteworthy that similar to the case of correlated disordered array, transmission gap also appears for uniform random systems despite the absence of any spatial correlation with the periodic array. To ensure the generality of the findings, we have taken the configurational average of four different random configuration and the corresponding reflectance and transmittance spectra are shown in the error bar plot of Fig. 4.2. Again, for correlated weakly disordered array ($\zeta = 0.1423$), the signature of periodic array is evident in the transmittance spectra. As a result, FP resonance modes can be seen in the spectra. This similarity in FP resonance peaks is marked with black and red circles for periodic and weakly correlated random arrays respectively. But, for correlated strongly disordered array, no such peaks

are visible. Again, as the disorder strength is increased, light transmission at the passband wavelengths decreases gradually. This reduction in transmittance is actually associated with the increase of scattering which will be detailed in the later section.

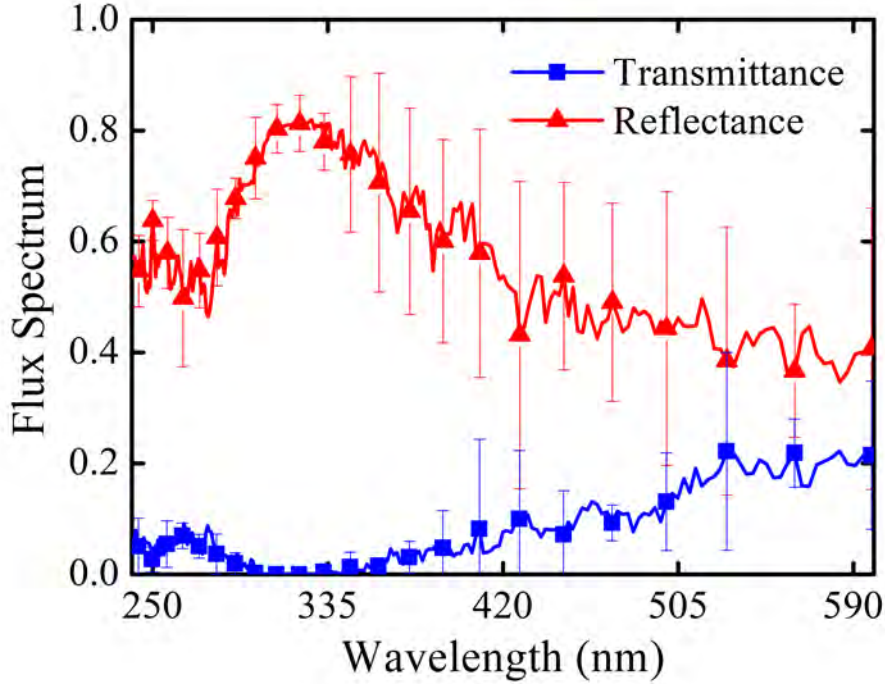


Figure 4.2: Reflectance and transmittance spectra for uniform random systems. Here, configurational average of four different random configurations with identical diameter and ff of 70 nm and 50% are shown.

From the sustainability and shrinkage of transmission gaps in the disordered systems, it can be interpreted that both Bragg and Mie process are involved in the gap formation process. As Bragg process is governed by the collective scattering of light from an array, long range periodicity is required for this process. As a result, the lack of periodicity in random systems results in a shrinkage of the gap. However, long range periodicity is not mandatory for Mie process as it is associated with the coupling of adjacent scatterers [41]. Hence, Mie gap can sustain disorder which results in the existence of gap even in completely random arrays. To get an understanding of the contribution of these Bragg and Mie process in gap formation

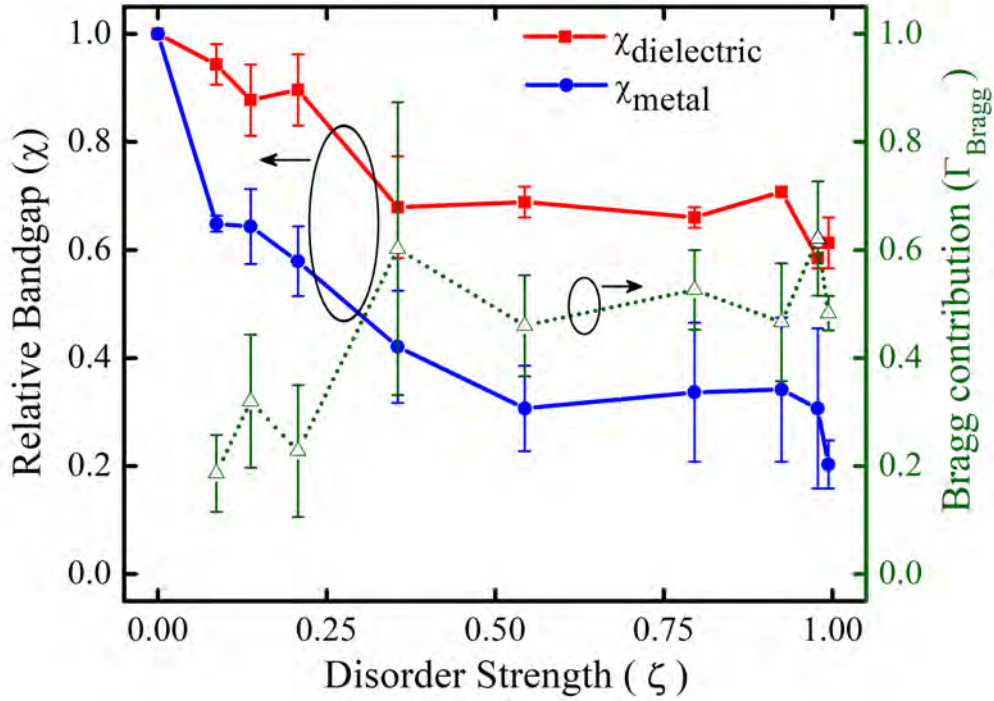


Figure 4.3: Relative bandgap (χ) as a function of disorder strength (ζ) for correlated disordered arrays. Percentage of Bragg contribution in bandgap formation process is also shown.

process, we have used the following equation [41]:

$$\Gamma_{\text{Bragg}} = \frac{1 - \chi^{\text{dielectric}}}{1 - \chi^{\text{metal}}} \quad (4.2)$$

Here, Γ_{Bragg} indicates the percentage of Bragg contribution. $\chi^{\text{dielectric}}$ and χ^{metal} denote the relative transmission gap for dielectric and metallic nanowire arrays with identical dimensions and spatial distributions. Relative transmission gap (χ) is defined as:

$$\chi = \frac{\Delta\lambda(\zeta)}{\Delta\lambda(0)} \quad (4.3)$$

According to the above equations, the calculated Γ_{Bragg} , $\chi^{\text{dielectric}}$, and χ^{metal} are plotted in Fig. 4.3. As can be seen from the figure, around 30% Bragg contribution is found for weakly disordered systems, which is in consistence with previous findings [41, 65]. But, for strongly disordered arrays ($\zeta \geq 0.4$) the dominance of Bragg contribution increases to around 57%. As a result, more gap shrinking is observed for strongly disordered arrays. Thus, both Bragg and Mie process are involved in

the gap formation process of our considered dielectric arrays.

4.1.2 Transmission gap tuning

The tunability of transmission gap for both periodic and random arrays are investigated in this section by controlling the diameters and fill-factors.

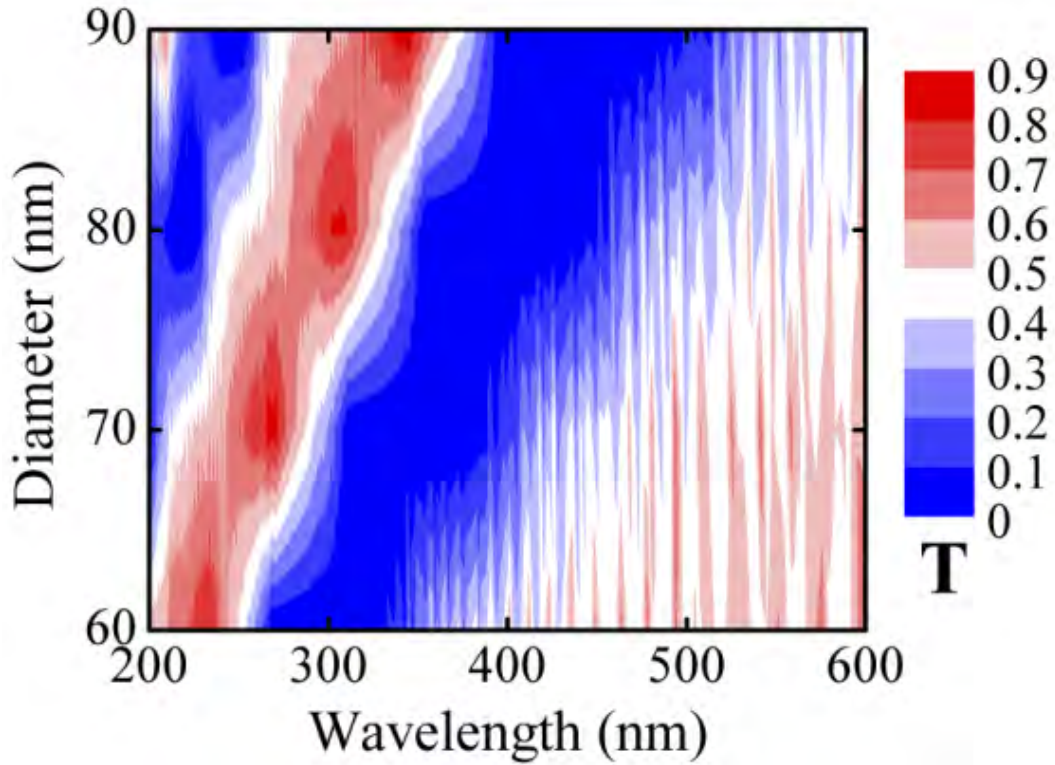


Figure 4.4: Contour plot of transmittance in periodic arrays for different diameters of the nanowires. Fill-factor is kept constant at 50 % in each case.

4.1.2.1 Effects of variation in diameters

Keeping the fill-factor fixed at 50 %, diameter is varied from 60 nm to 90 nm for the periodic systems and the corresponding transmittance spectra are observed. As can be seen from the contour plot of Fig. 4.4, transmission gap shifts towards longer wavelength along with an increase in diameter and the bandwidth of the gap also increases from about 52 nm to 82 nm for a change in diameter from 60 nm to 90 nm.

Now, the effects of diameter variation in disordered arrays is observed similar to that of periodic array. Similar trend of center wavelength of the TM gap being

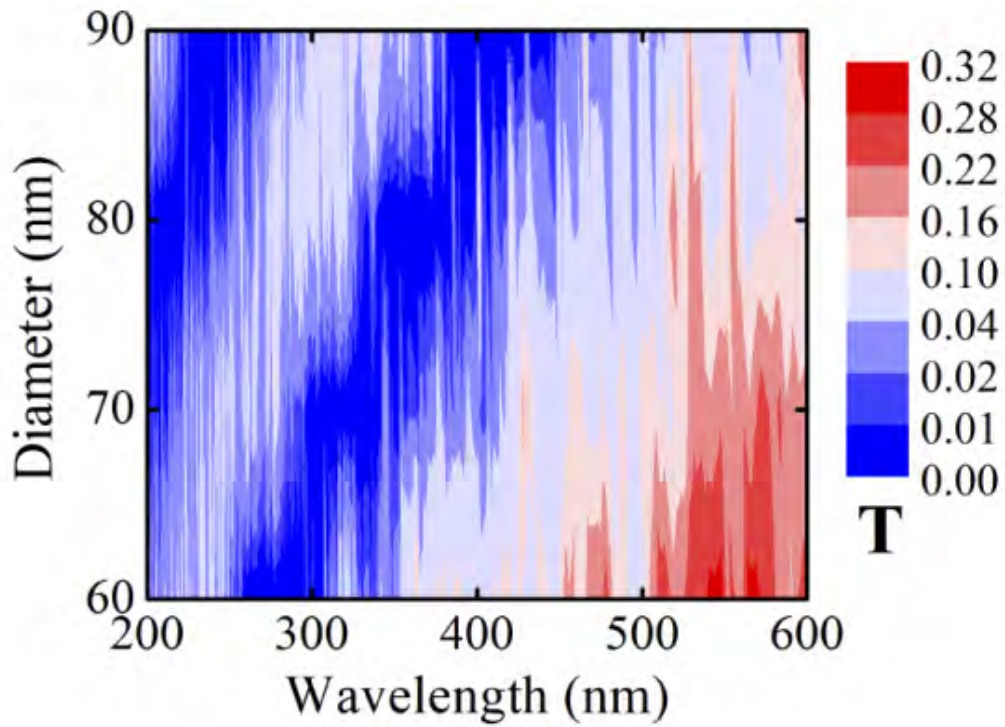


Figure 4.5: Contour plot of transmittance in random arrays for different diameters of the nanowires. Fill-factor is kept constant at 50% in each case.

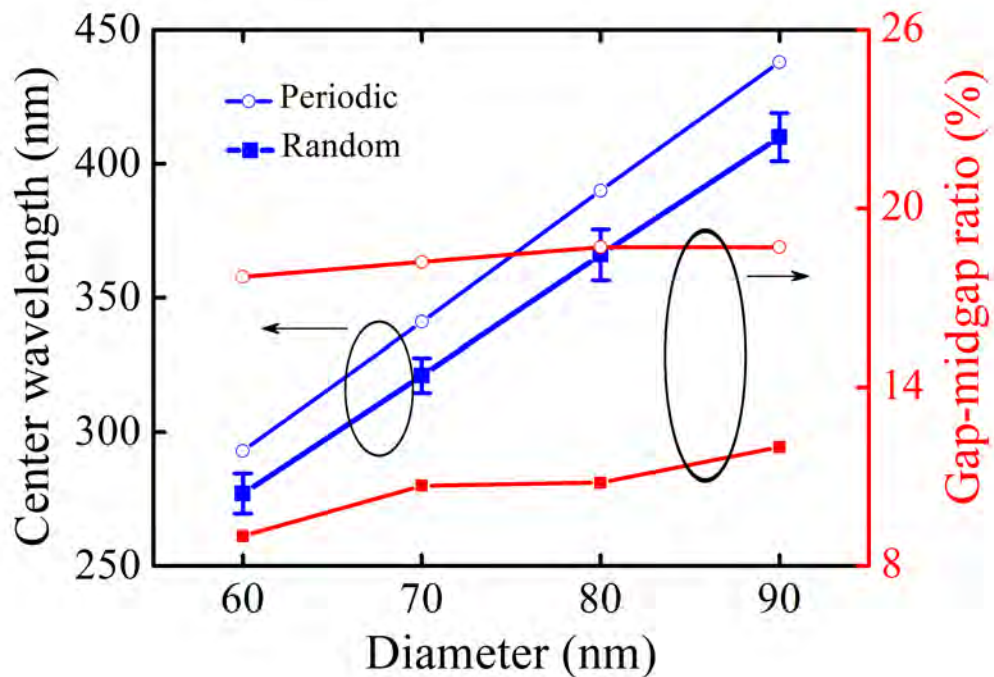


Figure 4.6: Variation of center wavelength of the transmission gap and gap-midgap ratio as a function of diameters for both periodic and random arrays.

shifted towards longer wavelength along with the increment of diameter is found in this case also as can be seen in the contour plot of Fig. 4.5. Here a shifting from 277 nm to 410 nm for center wavelength and an increase from 25 nm to 49 nm for gap size is observed by changing the diameter from 60 nm to 90 nm.

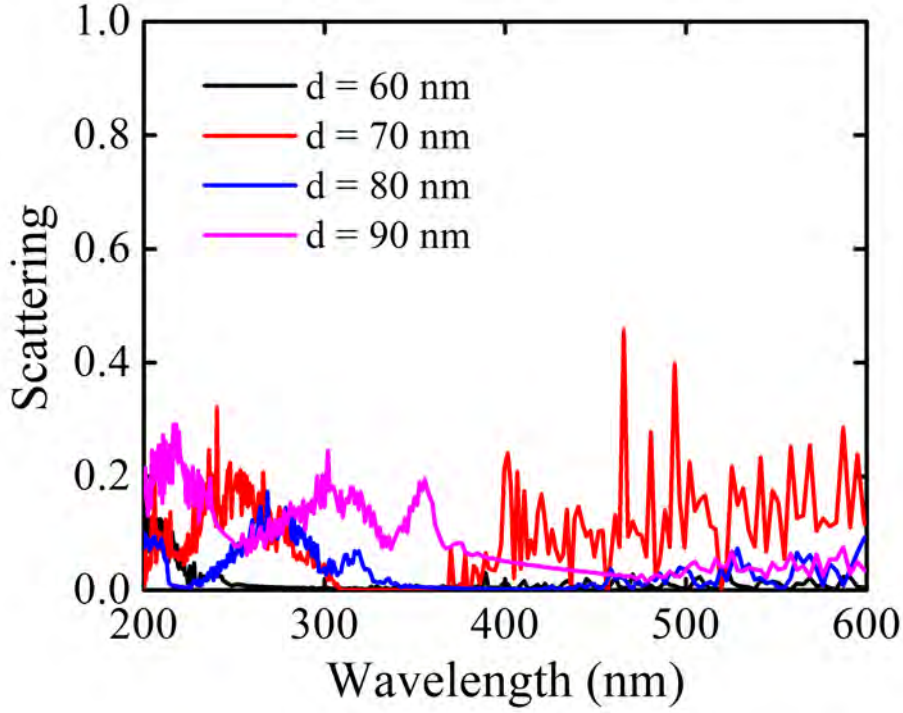


Figure 4.7: Scattering in periodic arrays for different diameters of the nanowires. Fill-factor is kept constant at 50 % in each case.

The variation of gap center and gap-midgap ratio along with diameter in both periodic and random structures is illustrated in Fig. 4.6. Four different sets of random structures with 50 %ff are studied for each diameter from 60 nm to 90 nm and the center wavelength of the gap is determined by taking the configuration average. It is observed from the figure that center wavelengths for both periodic and random structures increases linearly with diameter provided the ff is kept constant. But, gap centers for periodic structures are found to be at longer wavelengths for all the diameters in comparison to the random structures. Consequently, the gap-midgap ratios are also higher for periodic arrays at all the diameters. While gap-midgap ratio for the periodic systems remained around 18 % for all the cases, it increases slightly from $\sim 9\%$ to $\sim 11\%$ with an increase in diameter from 60 nm to 90 nm for the random arrays.

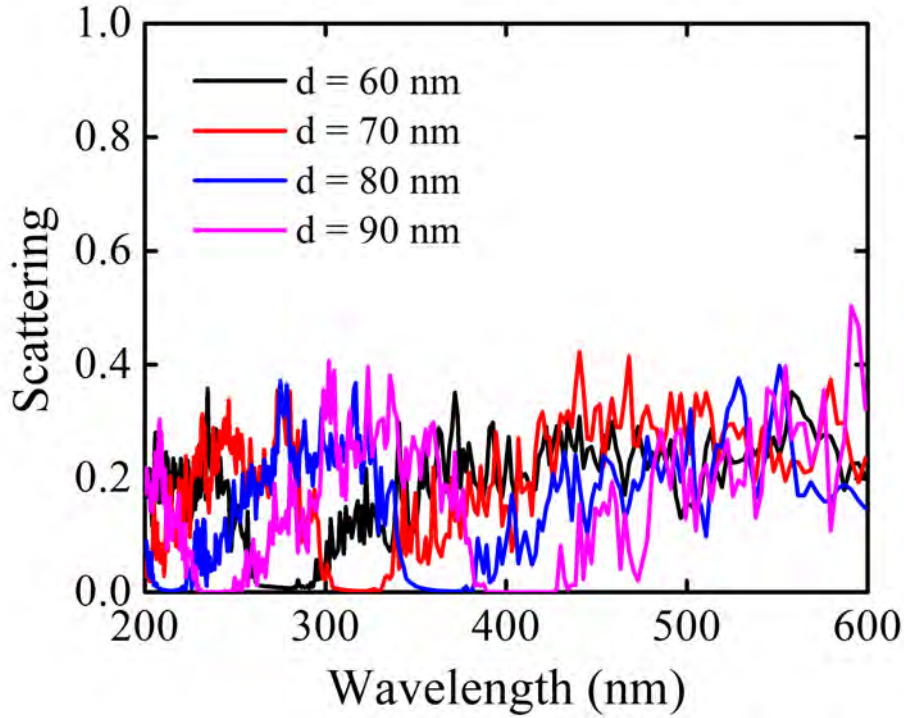


Figure 4.8: Scattering in random arrays for different diameters of the nanowires. Fill-factor is kept constant at 50 % in each case.

Now, to understand this shifting of transmission gap, the scattering fluxes through sideways (perpendicular to the direction of propagation) are recorded. The corresponding scattering spectra are plotted at different diameters of the arrays for both periodic and random structures in Figs. 4.7 and 4.8 respectively. From the figures, a shifting of zero scattering region along with diameter similar to the transmission gap can be seen for both periodic and random arrays. As gap wavelengths are not allowed to enter the system area, no scattering of light through sideways is possible. So, this phenomenon of gap shifting with diameter can be explained with the relation, $a = \sqrt{0.25\pi d^2/ff}$. As the diameter is increased, keeping the fill-factor constant, the effective lattice constant of the array increases. As a result, according to the dispersion relation, a shifting of the gap towards longer wavelengths is observed.

4.1.2.2 Effects of variation in fill-factors

Keeping diameter the same at 70 nm, fill-factor is changed from 30 % to 50 % to observe the effects of ff variation in periodic array. As evident from the plot

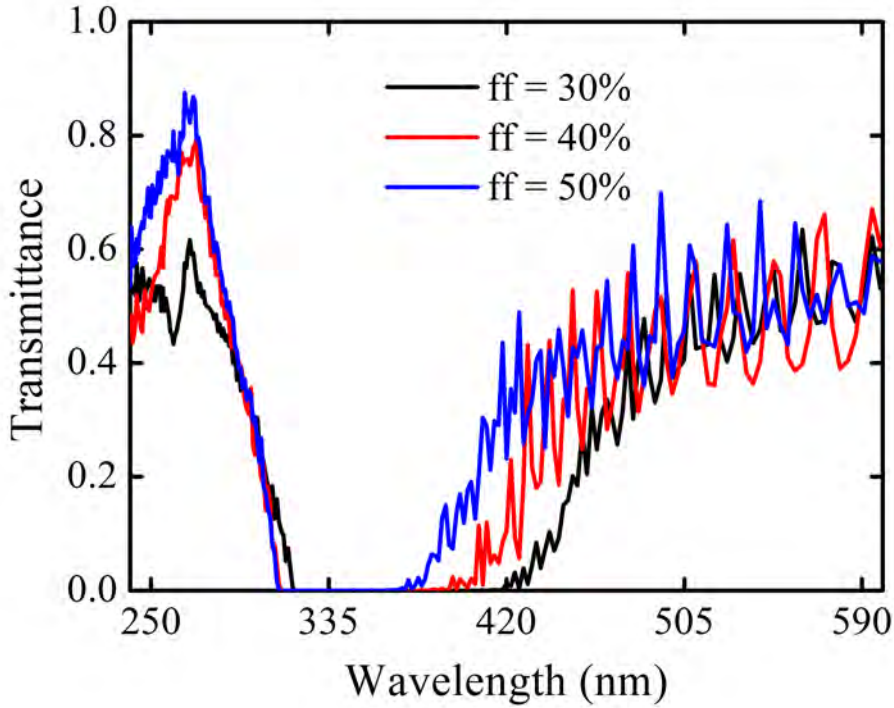


Figure 4.9: Transmittance spectra of periodic arrays at different fill-factors with the diameter being fixed at 70 nm in each case.

of Fig. 4.9, upon increasing the ff from 30 % to 50 %, a shifting toward shorter wavelength is found for the upper boundary of the gap while the lower boundary barely changed. As a result, gap size is reduced and center wavelength also shifted towards shorter wavelength from 367 nm to 341 nm along with a significant change in the gap-midgap ratio from 27 % to 18 %.

A similar study is conducted for random arrays by changing ff from 30 % to 50 % for 70 nm diameter in all cases. From the transmission spectra of Fig. 4.10, it can be clearly depicted that the highest value of transmittance is around 20 % for 50 % ff and it decreases below 10 % for 30 % ff. Similar to periodic array, a shifting of the center of the gap towards shorter wavelength from 352 nm at 30 % fill-factor to 321 nm at 50 % fill-factor and a change in gap-midgap ratio from 18 % to 11 % for similar change in fill-factor is found for random structures also. Along with that, a shrinkage of the gap size (from 66nm to 30nm) from upper wavelength of gap boundary is also observed for a change in ff from 30 % to 50 %.

The comparison of the characteristics of the transmission gap of periodic and random arrays in terms of center wavelength and gap-midgap ratios are also

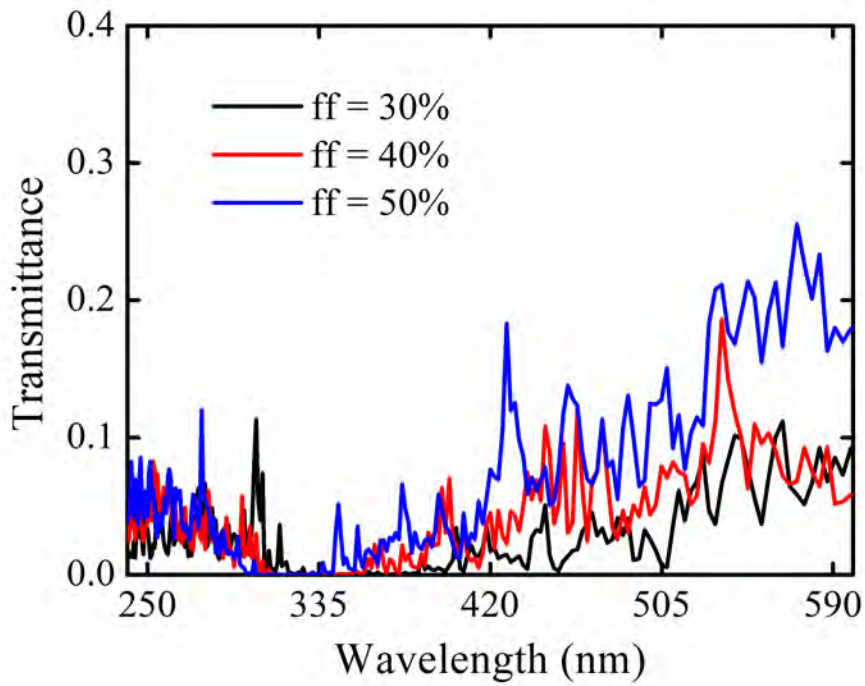


Figure 4.10: Transmittance spectra of random arrays at different fill-factors with the diameter being fixed at 70 nm in each case.

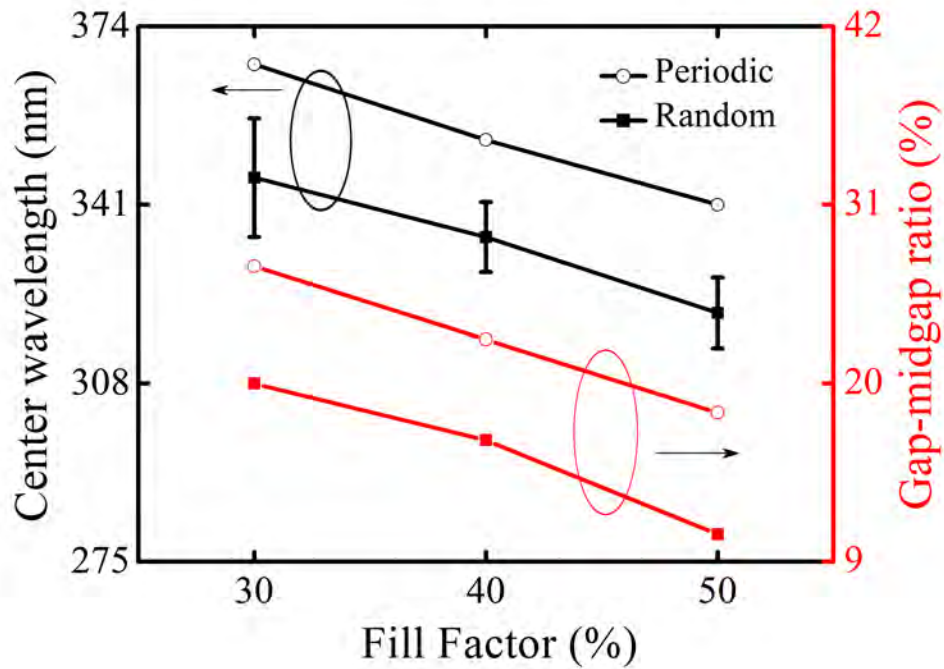


Figure 4.11: Variation of center wavelength of the transmission gap and gap-midgap ratio as a function of fill-factors for both periodic and random arrays.

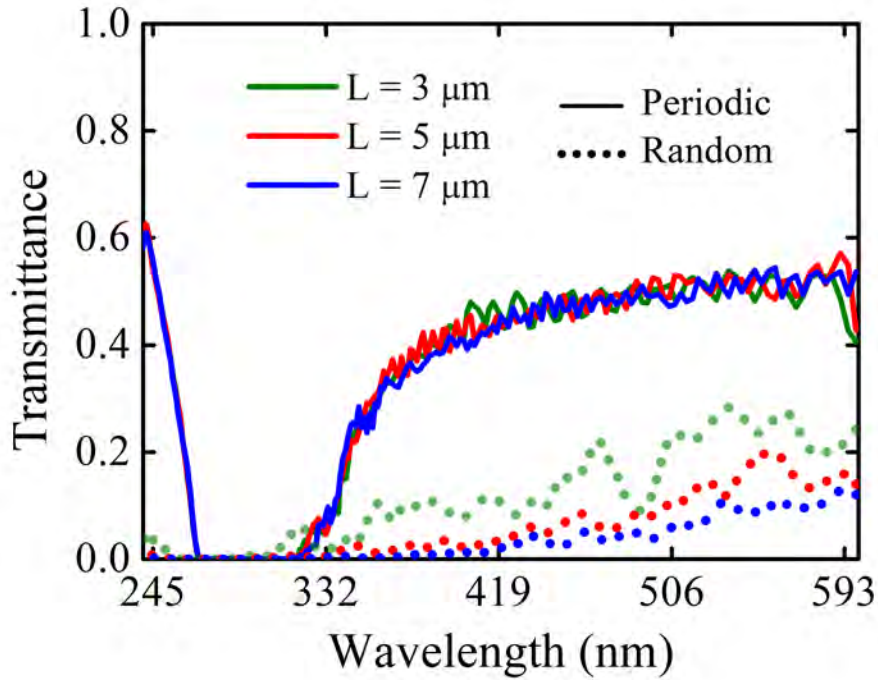


Figure 4.12: Transmittance spectra at different system lengths (L) for both periodic and random systems.

represented in Fig. 4.11. Though both center wavelengths and gap-midgap ratios are decreased with the increase of fill-factor in both periodic and random structures, the gap centers are always at longer wavelengths and gap-midgap ratios are also greater for the periodic arrays.

4.1.3 Effects of system length

4.1.3.1 Comparison of transmittance

Transmittance spectra for both periodic and random arrays are observed for different system lengths (L). Keeping the width of the systems at $3 \mu\text{m}$, length is varied from $3 \mu\text{m}$ to $7 \mu\text{m}$. The recorded spectra for both periodic and random arrays with 60 nm diameter and 50% ff are shown in Fig. 4.12. Five points moving average is used to reduce the excessive fluctuation so that the observation of the trend becomes easier. It is obvious from the plot here that transmittance in periodic structure is not variant to change in system length, while a gradual decrease of transmittance with larger L is found for random systems. In addition to that, the value of transmittance beyond the transmission gap region is found to be around

50 % for periodic arrays, but for random arrays it remained around 20 %.

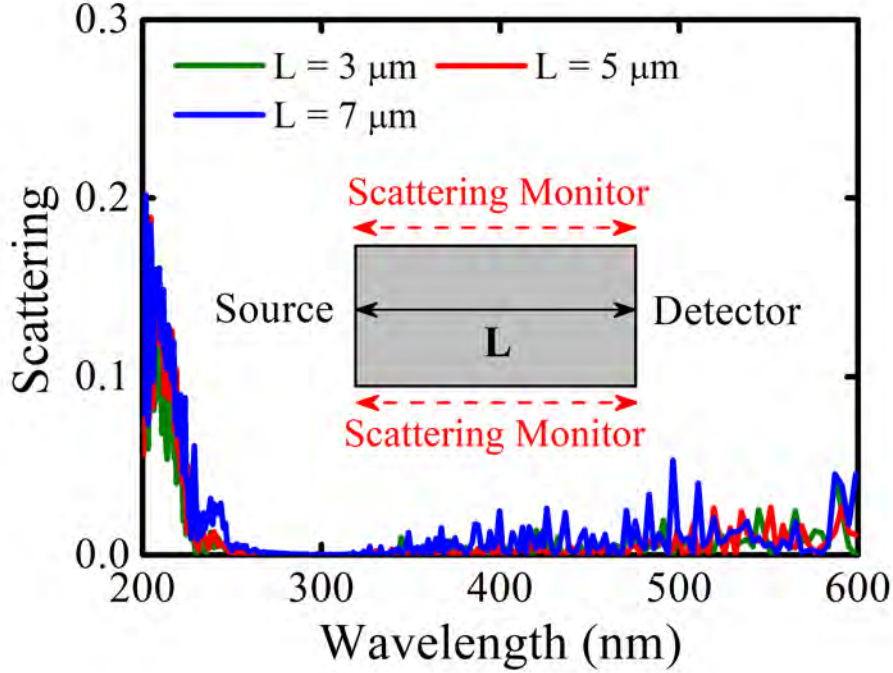


Figure 4.13: Scattering spectra at different system lengths (L) for periodic systems. The location of scattering monitors to record the scattered flux is also shown in the inset.

4.1.3.2 Light scattering

To understand the lower value of transmittance in random arrays, we studied the scattering of light for different system lengths in both periodic and random structures. Two power monitors of the same length of the system are placed along the two sides of the array to record the scattered light from the system. Normalizing with the input power, the recorded values of both the monitors are added together to get the total scattering out of the system. Scattering for the periodic and random systems of different lengths with 60 nm diameter and 50 % ff are illustrated graphically in Figs. 4.13 and 4.14 respectively. A schematic of the setup is also shown in the inset of Fig. 4.13. As can be seen from the figure, the value of scattering for periodic structures are around 2 % beyond the transmission gap and it remains the same irrespective of the system lengths. But for the random arrays, scattering increases from $\sim 20\%$ at $3\ \mu\text{m}$ to $\sim 40\%$ at $7\ \mu\text{m}$ for wavelengths outside of the gap region. This dominance of scattering in the random systems explains

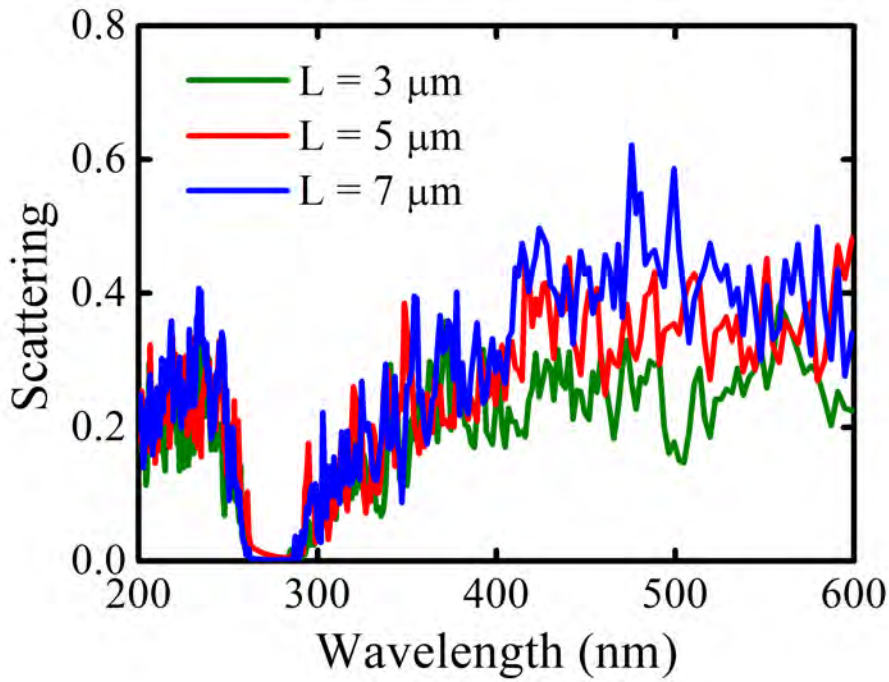


Figure 4.14: Scattering spectra at different system lengths (L) for random systems.

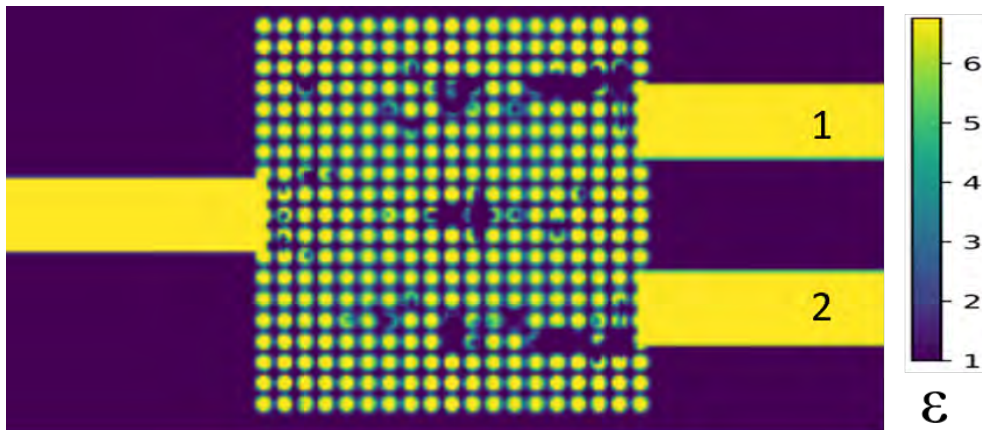


Figure 4.15: Optimized power splitter for 550 nm wavelength with periodic nanowire array initial structure.

the lower value of transmittance compared to the periodic ones at the passband wavelengths. Again, scattering at transmission gap wavelengths are almost zero for both periodic and random systems as light of these wavelengths are not allowed to enter the system area.

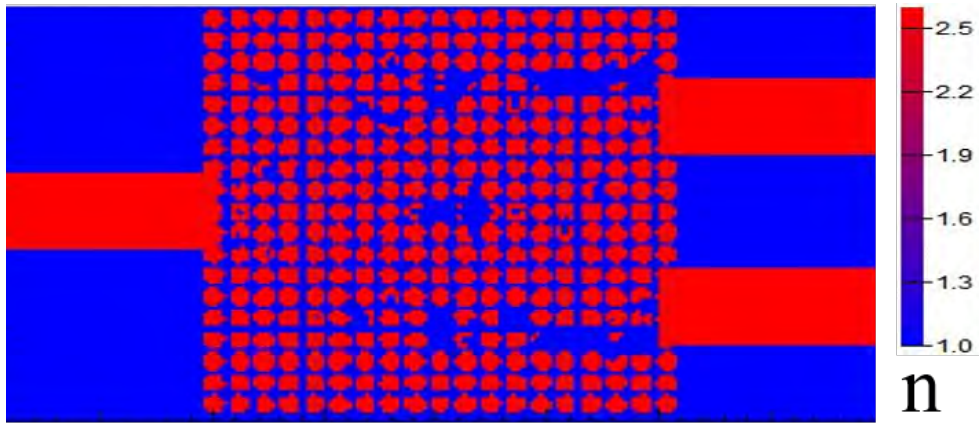


Figure 4.16: Discretized power splitter for 550 nm wavelength with periodic nanowire array initial structure.

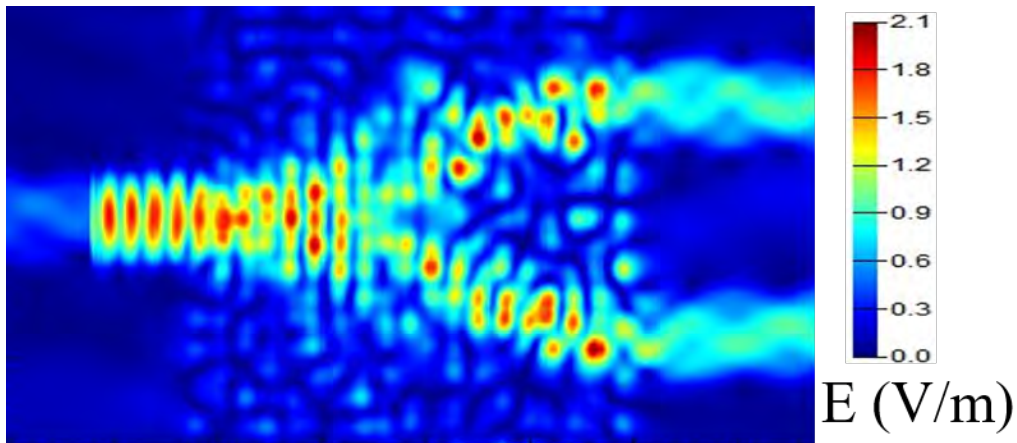


Figure 4.17: Electric field distribution at 550 nm wavelength of the designed power splitter with periodic nanowire array initial structure.

4.2 Disorder System Based Demultiplexers and Power Splitters

Based on the understanding of light transmission in random arrays, we have investigated the potential of such arrays in being used as power splitters and wavelength demultiplexers. Employing inverse design based optimization technique, we have proposed customized designs generated from periodic and random nanowire arrays in this section.

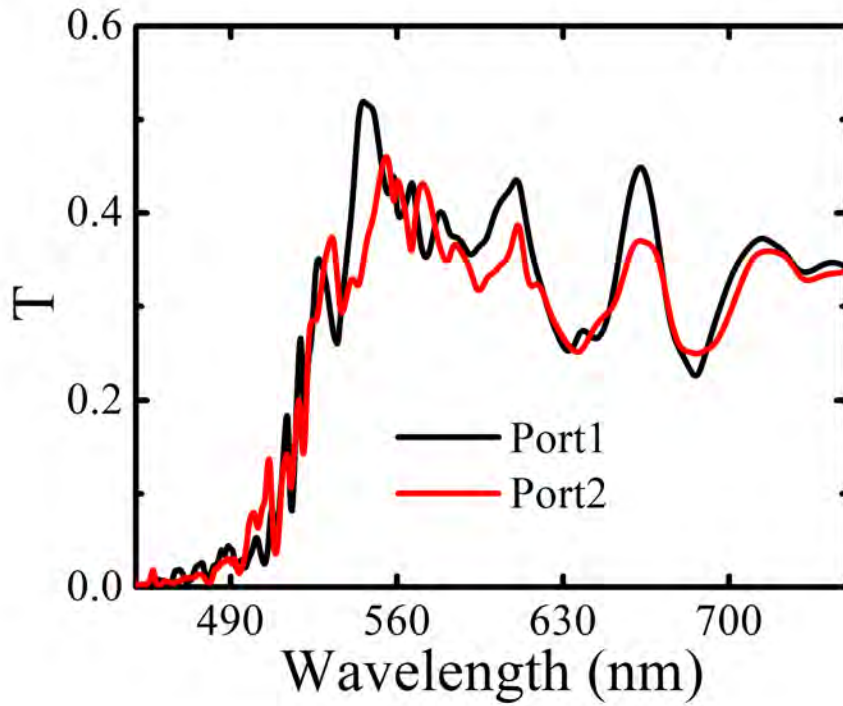


Figure 4.18: Transmittance spectra for the designed power splitter with periodic nanowire array initial structure.

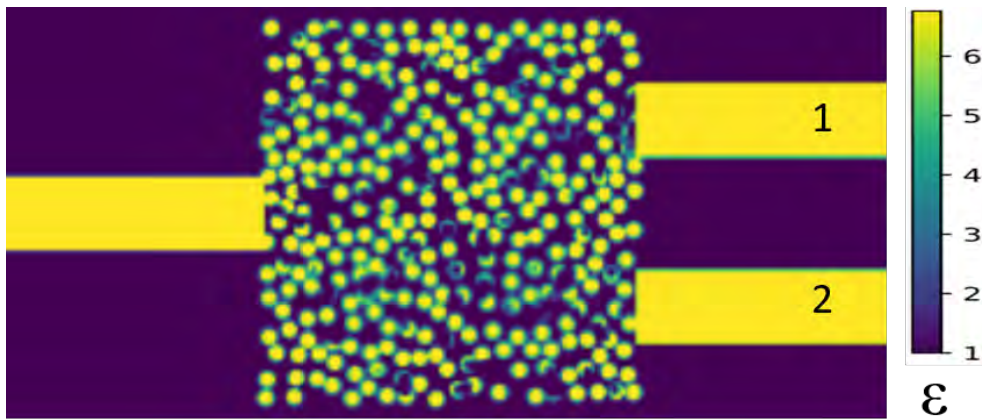


Figure 4.19: Optimized power splitter for 550 nm wavelength with random nanowire array initial structure.

4.2.1 Power splitters at 550 nm wavelength

For designing power splitter, the target is to maximize the power transfer at 550 nm wavelength to the output ports marked as port “1” and port “2” in Fig. 4.15. Taking periodic nanowire array as the initial structure, the objective function is defined. Then adjoint optimization is run on the initial structure to generate an optimized permittivity distribution. In this step, the permittivity distribution is

allowed to vary continuously i.e. arbitrary index is allowed in between the indices of GaN and air medium. The optimized structure generated after the final iteration is shown in Fig. 4.15.

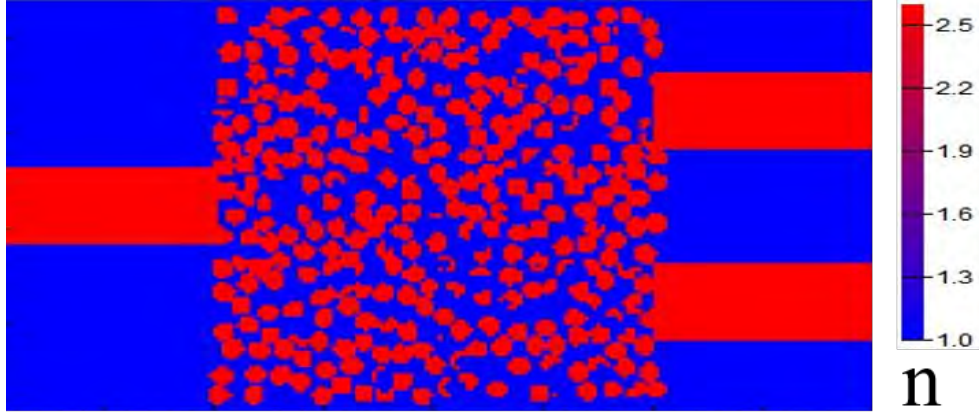


Figure 4.20: Discretized power splitter for 550 nm wavelength with random nanowire array initial structure.

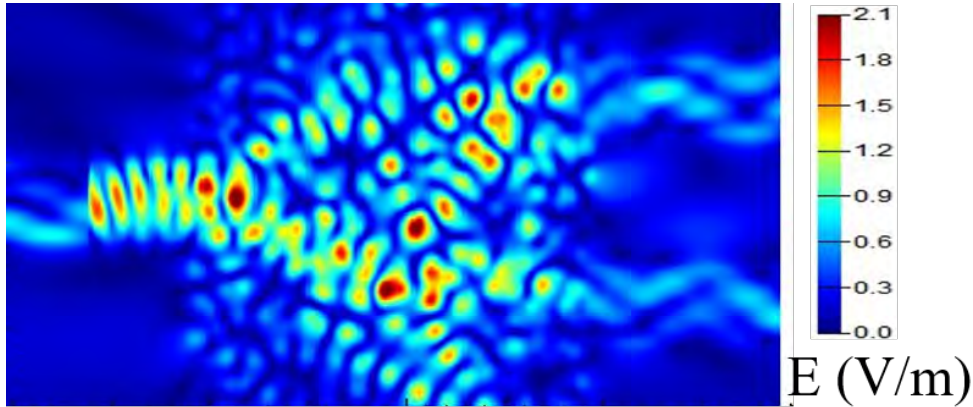


Figure 4.21: Electric field distribution at 550 nm wavelength for the designed power splitter with random nanowire array initial structure.

Now, as materials with arbitrary refractive index is not realizable, the generated structure is needed to be discretized. We have employed binary discretization technique as described earlier for generating the discretized structure, which is shown in Fig. 4.16. The discretized permittivity distribution is then imported in Lumerical to run finite difference time domain simulation on the final design. Injecting a gaussian shape broadband mode source from the left port, transmittance is recorded at both the output ports. As can be seen from the electric field distribution of Fig. 4.17, power is splitted at both the output port for 550 nm wavelength. Corresponding transmittance spectra is shown in Fig. 4.18. As evident from the

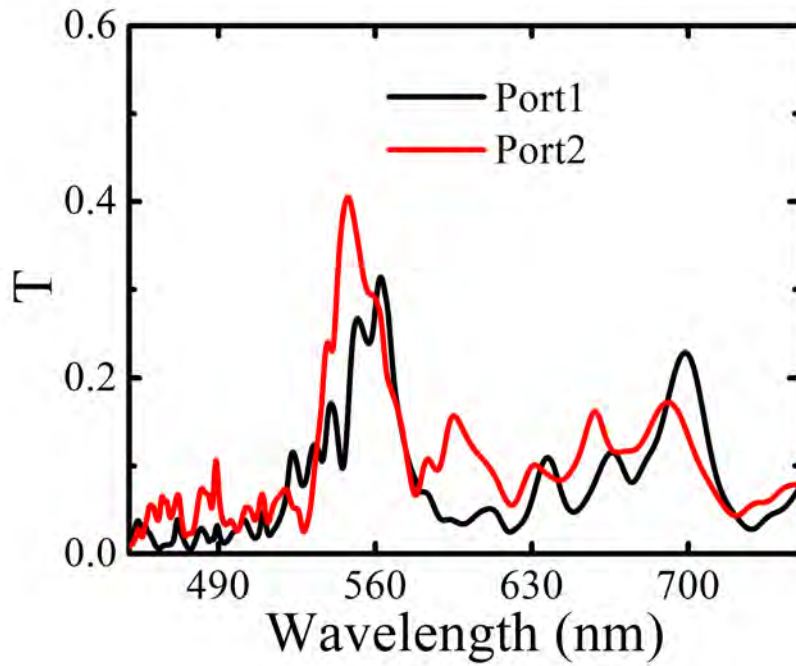


Figure 4.22: Transmittance spectra for the designed power splitter with random nanowire array initial structure.

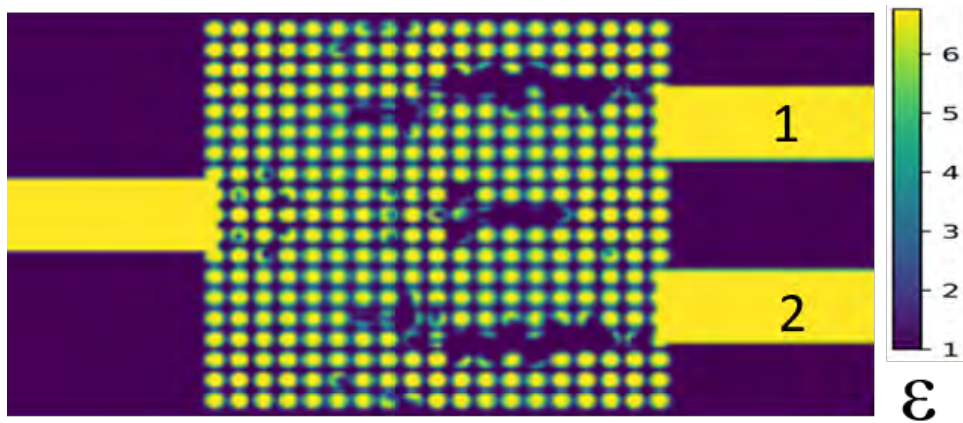


Figure 4.23: Optimized power splitter for 650 nm wavelength with periodic nanowire array initial structure.

figure that transmittance at port1 and port2 are 52 % and 44 %, respectively, which are very close to the ideal value of 50 %.

Similarly for the random nanowire array initial structure, the objective function is defined to maximize the power transfer for 550 nm wavelength at both the output port. The optimized structure in this case is shown in Fig. 4.19. Now, to generate a physically realizable structure, binary discretization technique is used. The discretized permittivity distribution is presented in Fig. 4.20. Importing this

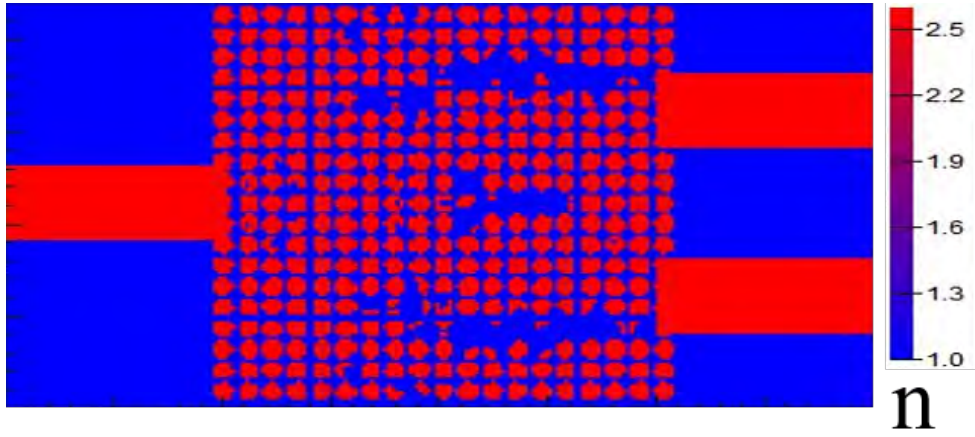


Figure 4.24: Discretized power splitter for 650 nm wavelength with periodic nanowire array initial structure.

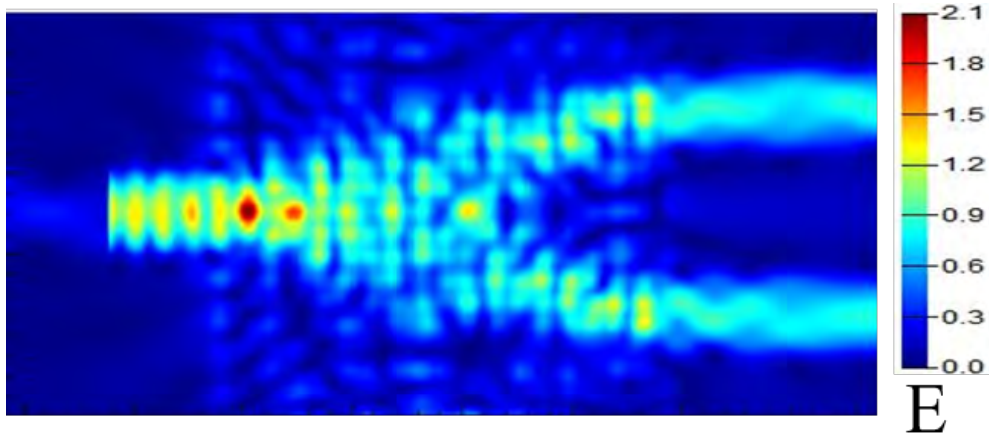


Figure 4.25: Electric field distribution at 650 nm wavelength of the designed power splitter with periodic nanowire array initial structure.

discretized structure in Lumerical, FDTD simulation is carried out to get the field distribution and transmittance spectra which are shown in Figs. 4.21 and 4.22 respectively. As evident from the figure, transmittance at port1 and port2 are 26 % and 40 % respectively. As the overall transmittance at 550 nm wavelength is lower for random nanowire array initial structure due to increased scattering through sideways, a lower value of transmittance is found with random array compare to the transmittance with periodic array.

4.2.2 Power splitters at 650 nm wavelength

To design a power splitter for 650 nm wavelength, the objective function should be changed to maximize the power transfer at the output ports for 650 nm

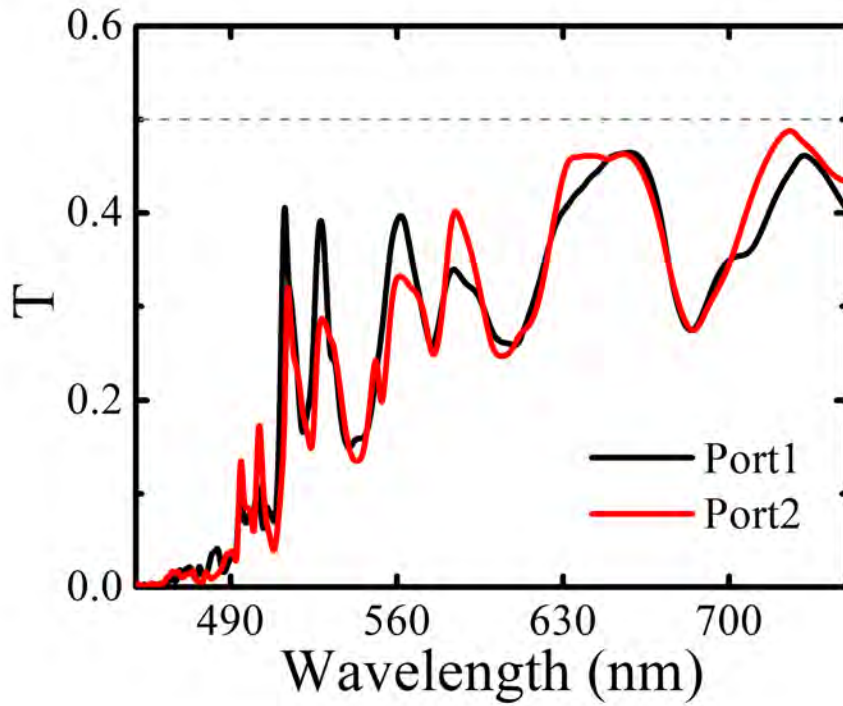


Figure 4.26: Transmittance spectra for the designed power splitter with periodic nanowire array initial structure.

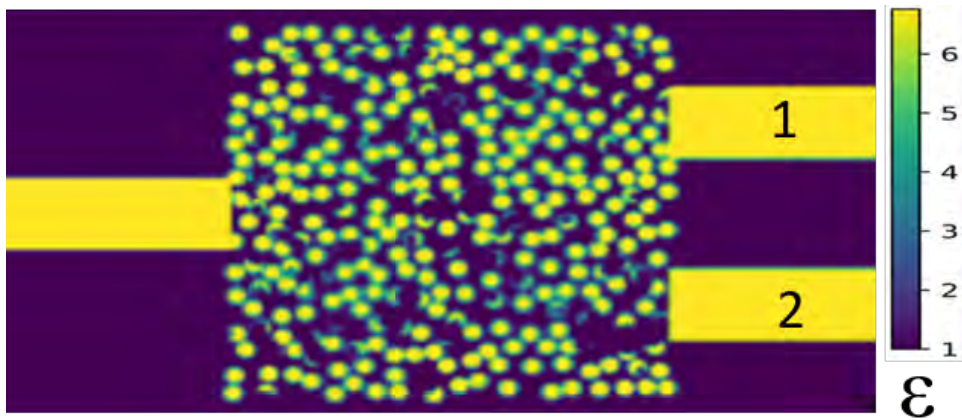


Figure 4.27: Optimized power splitter for 650 nm wavelength with random nanowire array initial structure.

wavelength. Setting the objective properly, optimization is run for periodic nanowire array initial structure and the generated permittivity distribution is shown in Fig. 4.23. The result of this continuous optimization is discretized to get the design of Fig. 4.24. Again, discretized permittivity is imported in Lumerical to get the E field distribution and transmittance spectra of Figs. 4.25 and 4.26. From these figures, it can be seen that power is splitted almost equally to both the output ports and

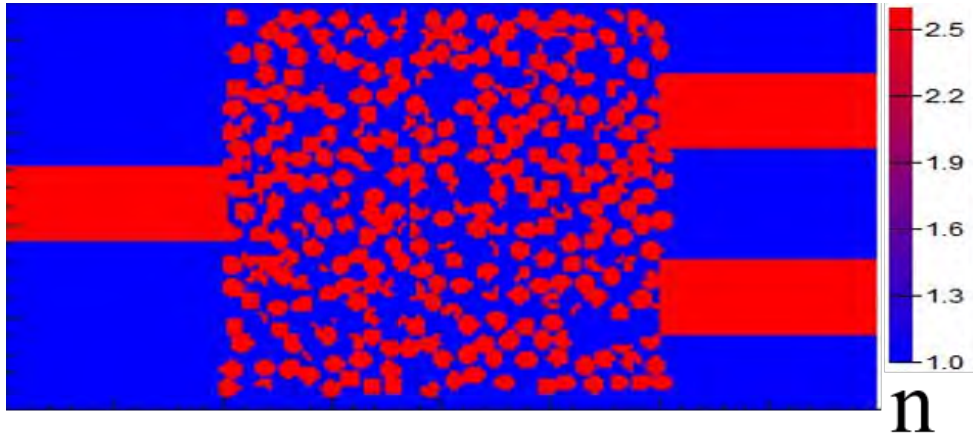


Figure 4.28: Discretized power splitter for 650 nm wavelength with random nanowire array initial structure.

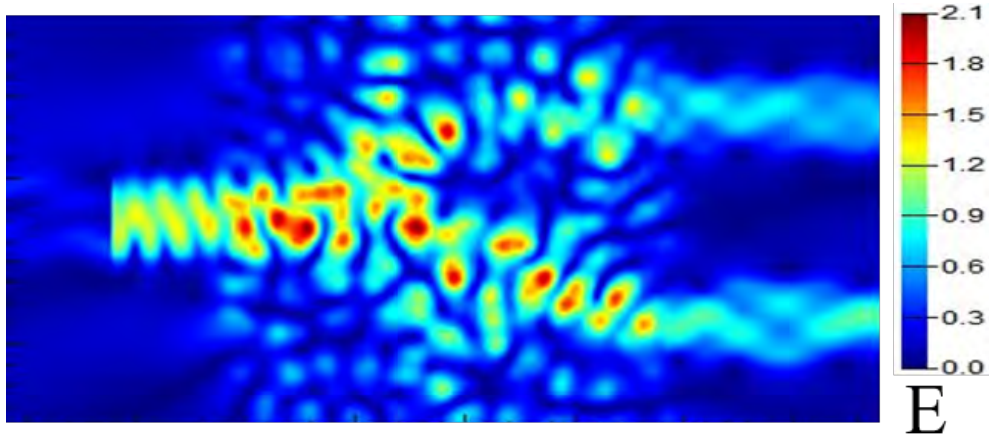


Figure 4.29: Electric field distribution at 650 nm wavelength for the designed power splitter with random nanowire array initial structure.

the recorded transmittance of $\sim 46\%$ at both the ports are very close to the ideal value of 50% .

Similarly, for the random nanowire array initial structure, optimization objective is set to maximize the power transfer at 650 nm wavelength and the optimized result of the final iteration is shown in Fig. 4.27. Result of this continuous optimization is discretized to get the permittivity distribution of Fig. 4.28. Importing this discretized distribution in Lumerical, FDTD simulation is run to get the E field distribution and broadband transmittance spectra of Figs. 4.29 and 4.30 respectively. In this case, the transmittance at port1 and port2 are 40% and 53% respectively, which are comparable to the values obtained with periodic nanowire array initial structure.

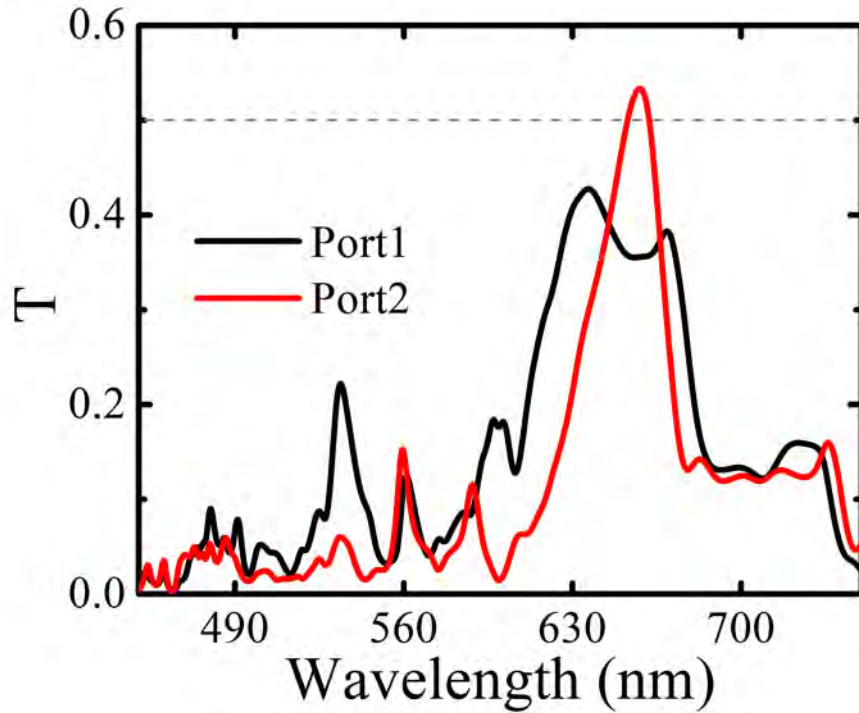


Figure 4.30: Transmittance spectra for the designed power splitter with random nanowire array initial structure.

Now, different random data sets with identical dimensions are considered for the optimization based on the defined objective function and the corresponding transmittance spectra are recorded by running FDTD simulation on the discretized structures. The results of these power splitters at both 550 nm and 650 nm wavelengths are summarized in Table 4.1. It can be noted that the performance of all the random structures are comparable with periodic structure in terms of splitting 650 nm wavelength. But, random structure5 outperforms other random structures in terms of splitting 550 nm wavelength.

4.2.3 WDM at 550 and 650 nm wavelengths

Wavelength demultiplexer is designed to pass light of 650 nm wavelength to port1 and 550 nm wavelength to port2. The objective function is set to maximize the power transfer of 550 nm wavelength to port2 while minimizing it through port1. Similarly, power transfer of 650 nm wavelength is intended to be maximized to port1 and minimized to port2. Taking periodic nanowire initial structure, optimization is run by setting the objective function as described earlier. The generated structure

Table 4.1: Comparison of transmittance for the designed power splitters.

Structure	Transmittance			
	At 550 nm		At 650 nm	
	Port1	Port2	Port1	Port2
Periodic	52 %	44 %	46 %	46 %
Random structure1	26 %	40 %	40 %	53 %
Random structure2	31 %	46 %	51 %	42 %
Random structure3	54 %	31 %	47 %	42 %
Random structure4	39 %	45 %	44 %	40 %
Random structure5	42 %	46 %	45 %	41 %

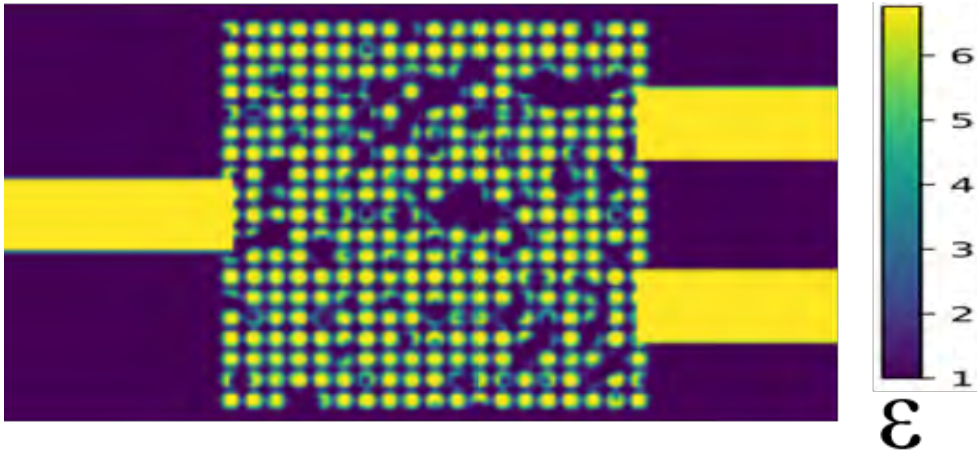


Figure 4.31: Optimized demultiplexer structure for periodic nanowire array initial structure.

after running the iterations of continuous optimization is shown in Fig. 4.31. The discretized structure generated after binary optimization is presented in Fig. 4.32. Importing this discretized permittivity distribution, FDTD simulation is carried out to get electric field distribution and transmittance spectra as shown in Figs. 4.33 and 4.34 respectively. It is evident from the figure that the transmittance for 550 nm wavelength is 74 % through port2, while it is only 1.8 % through port1. Similarly, transmittance for 650 nm wavelength is maximized to 83 % to port1, while it is minimized to 2.5 % to port2.

Now, random nanowire array is taken as the initial structure and the objective function is defined similarly for same set of wavelength as the periodic array. After

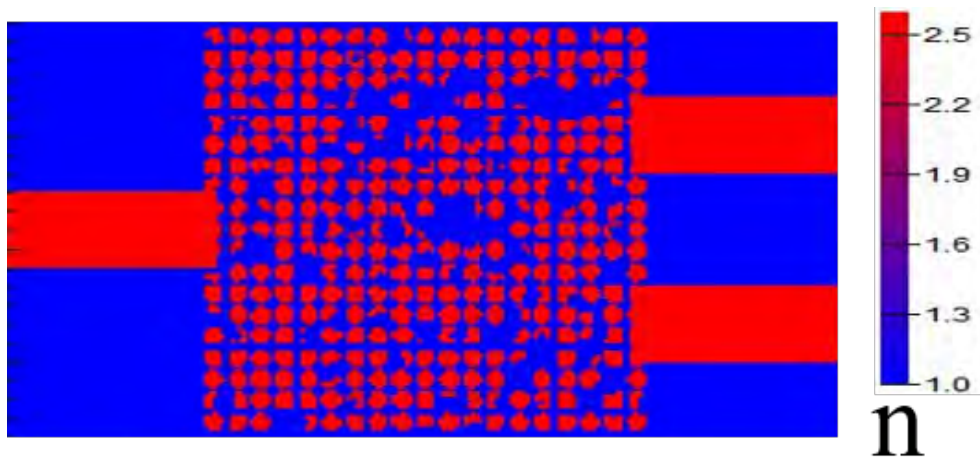


Figure 4.32: Discretized demultiplexer structure for periodic nanowire array initial structure.

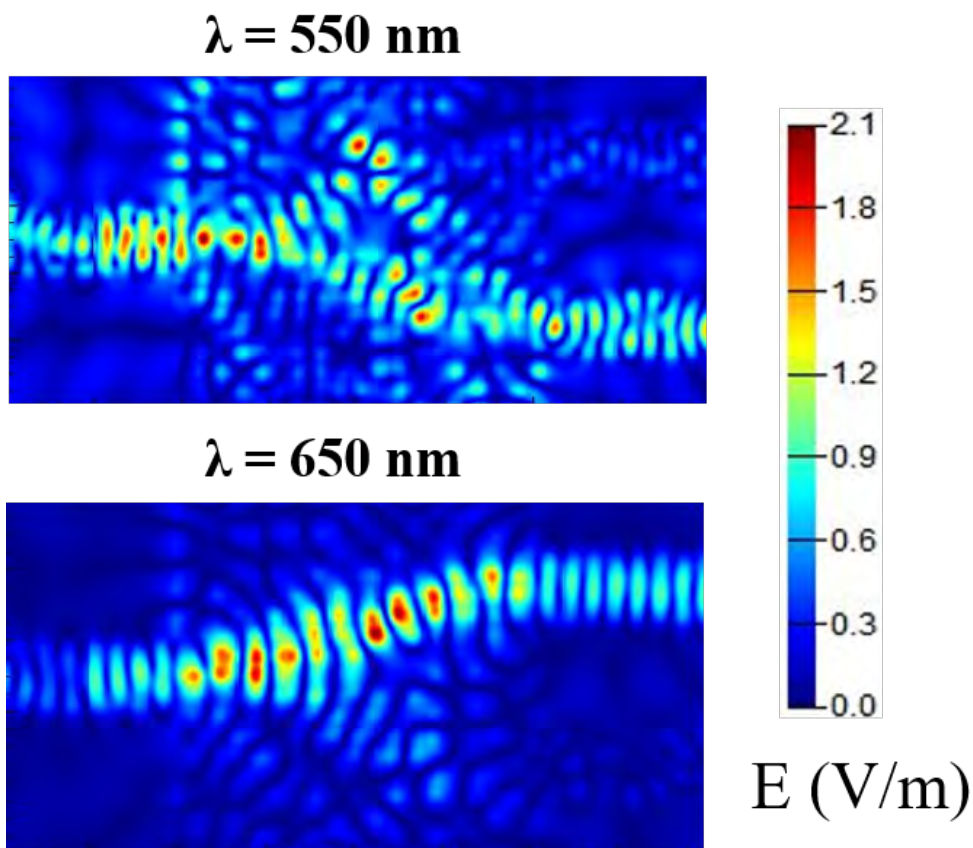


Figure 4.33: Electric field distributions at 550 nm (top) and 650 nm (bottom) wavelengths for the designed demultiplexer with periodic nanowire array initial structure.

running the optimization the structure of Fig. 4.35 is generated. The result of this continuous optimization is discretized similar to the previous ones to get the discretized structure of Fig. 4.36. FDTD simulation is carried out in this case

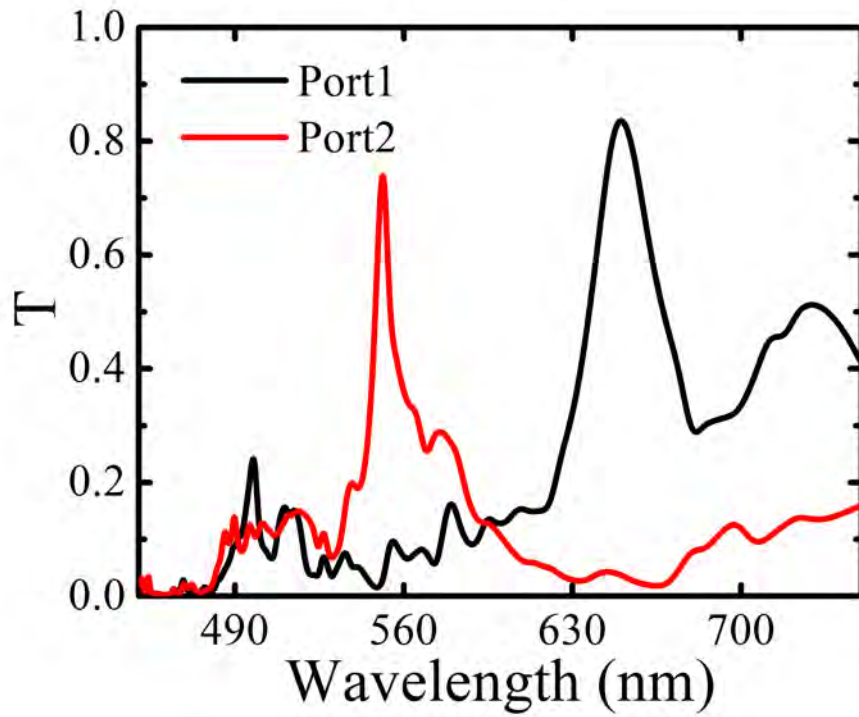


Figure 4.34: Transmittance spectra for the designed demultiplexer with periodic nanowire array initial structure.

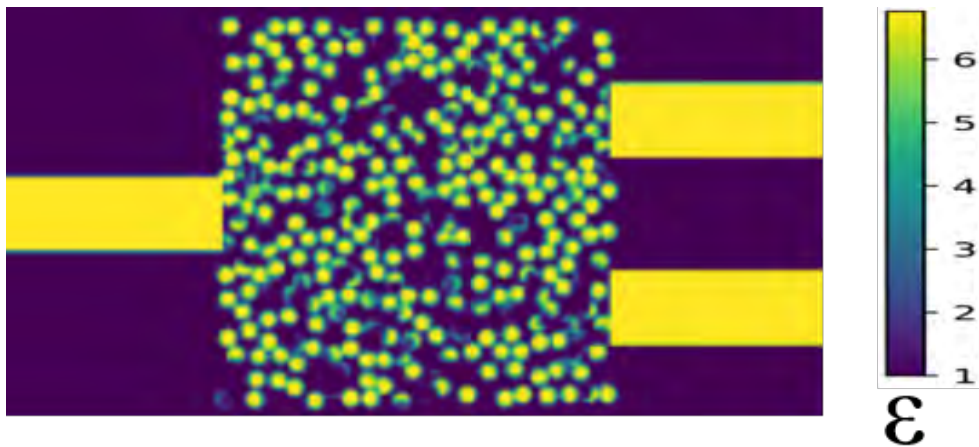


Figure 4.35: Optimized demultiplexer structure for random nanowire array initial structure.

also on the final design to observe the E field distribution and the transmittance spectra, which are presented in Figs. 4.37 and 4.38 respectively. In this case, the transmittance for 550 nm wavelength is found to be 78% to port2 while it is minimized to 1.7% to port1. Similarly, the transmittance for 650 nm wavelength is maximized to 82% to port1 while it is found to be only 0.7% to port2.

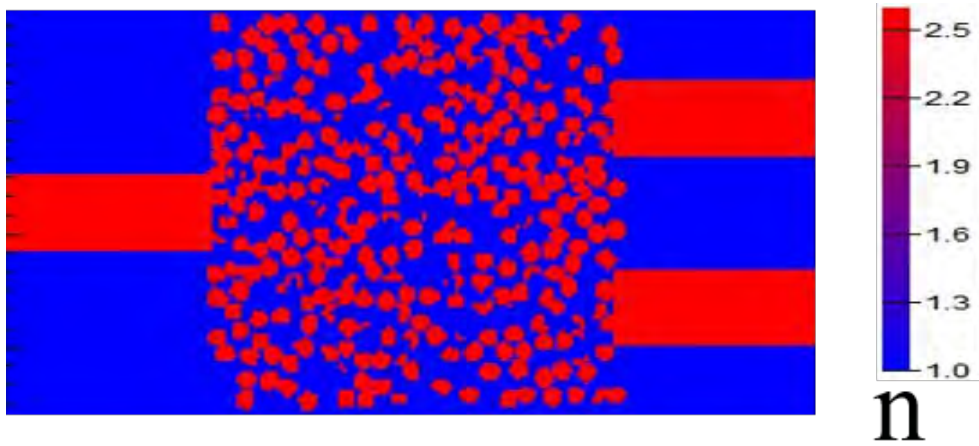


Figure 4.36: Discretized demultiplexer structure for random nanowire array initial structure.

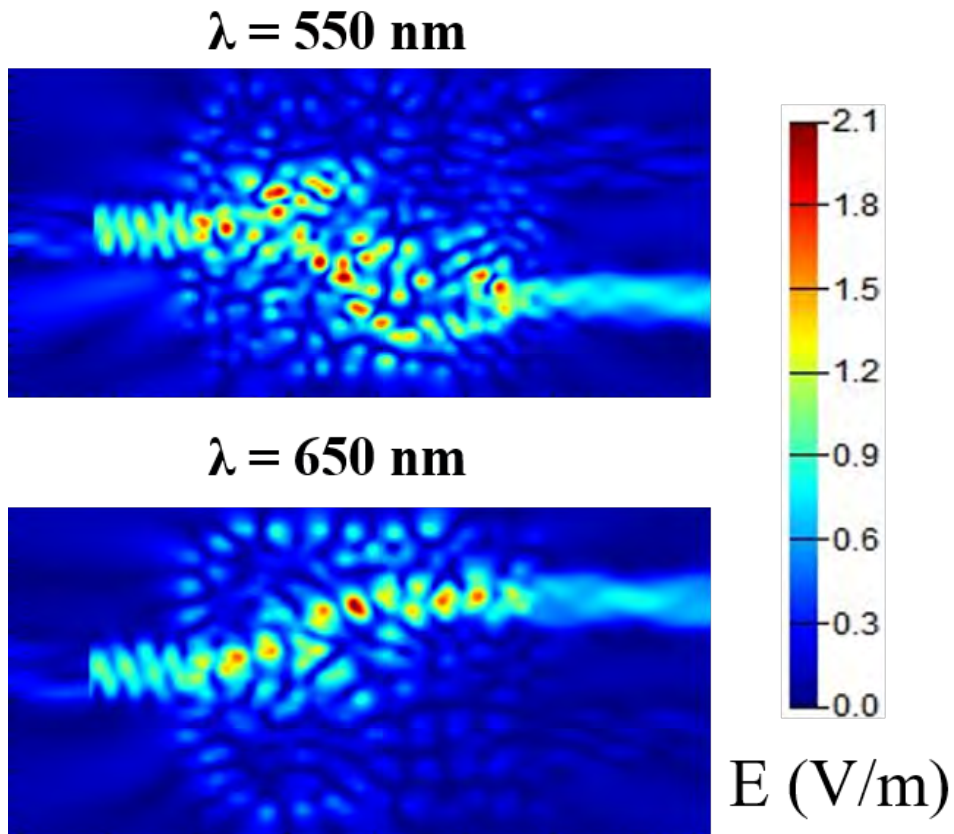


Figure 4.37: Electric field distributions at 550 nm (top) and 650 nm (bottom) wavelengths for the designed demultiplexer with random nanowire array initial structure.

Similarly, different random data sets with identical diameters and fill-factors are taken as the initial structures and optimization is run based on the defined objective function. Running the FDTD simulation, transmittance at both the port

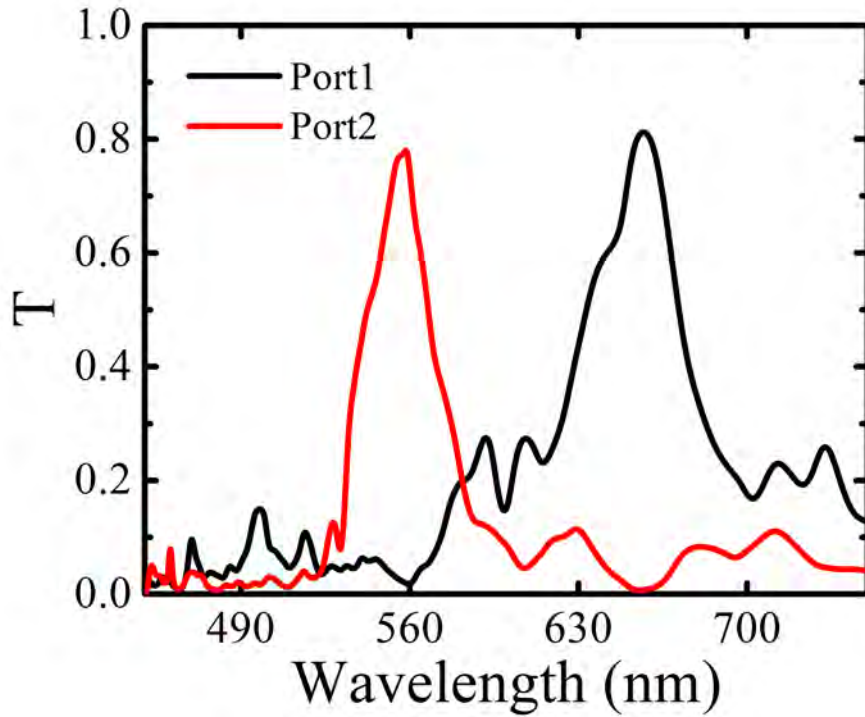


Figure 4.38: Transmittance spectra for the designed demultiplexer with random nanowire array initial structure.

Table 4.2: Comparison of transmittance for the designed wavelength demultiplexers.

Structure	Transmittance			
	At 550 nm		At 650 nm	
	Port1	Port2	Port1	Port2
Periodic	1.8 %	74 %	83 %	2.5 %
Random structure1	1.7 %	78 %	82 %	0.7 %
Random structure2	1.4 %	66 %	77 %	4.5 %
Random structure3	2.6 %	68 %	83 %	1.4 %
Random structure4	1.7 %	57 %	85 %	1.2 %
Random structure5	2.7 %	66 %	78 %	1.7 %

is recorded in each case. The summary of the performance of the designed WDMs are represented in Table 4.2. It is noteworthy from the comparison that random structure1 provides better performance in terms of transmitting 550 nm wavelength and random structure4 is better for transmitting 650 nm wavelength. But, overall

random structure1 is comparable to the periodic structure in terms of transmittance at both the ports.

Chapter 5

Conclusion

5.1 Summary

To summarize, we have investigated the light transmission characteristics in periodic, correlated weakly disordered, correlated strongly disordered, and uniform random arrays of dielectric nanowires. It is found that transmission gap arises in almost at the same wavelength region in such arrays that matches with the photonic bandgap of photonic crystals with identical diameters and fill-factors. The origin of transmission gap is also investigated and both Bragg and Mie process are found to be involved in the gap formation process in our systems. As Bragg process depends on the long range periodicity of the array, gap size shrinks with the increase of disorder strength. However, due to the involvement of Mie process, significant transmission gap is sustained in disordered array with the highest value of disorder strength. We have also found that similar to the case of correlated disordered array, transmission gap can be obtained in uniform random arrays where any form of spatial correlation with the periodic arrays are absent. The tuning of the transmission gap in both periodic and random systems is also obtained by varying the diameter and fill-factor of the arrays. It is noteworthy that transmission gap follows similar trend in both the systems. Whereas transmission gap shifts towards longer wavelength with an increase in diameter, blue-shifting of the gap is observed for an increment in fill-factor of the arrays.

We have also found that transmission of light at the passband wavelengths decreases with an increase in disorder strengths of the arrays due to an increase

in scattering of light through sideways. Again, transmission in periodic system is found to be invariant to system lengths, whereas it (transmission) decreases for random arrays as more light are scattered through sideways for longer arrays. Based on our understanding of light transmission, we have also designed power splitters and wavelength demultiplexers at passband wavelengths. Optimized power splitters for 550 nm and 650 nm wavelengths are designed by employing inverse design based optimization technique in both periodic and random nanowire arrays. Though power splitter designed based on periodic array outperforms that of random array at 550 nm wavelength, performance of both periodic and random systems are comparable for 650 nm wavelength. Similarly, inverse design technique is employed to design optimized wavelength demultiplexers that maximize the transfer of 550 nm wavelength through one output port and 650 nm wavelength through another. While transmittance for the WDM designed with periodic nanowire array are 74 % and 83 % for 550 nm and 650 nm wavelengths respectively, it (transmittance) is found to be 78 % and 82 % for the random nanowire array. To conclude, our study will enhance the understanding of disordered arrays and will simulate further study to implement photonic devices based on such random arrays.

5.2 Future Scopes

Our study may be extended further to a variety of applications that are briefly presented below:

- Due to resource limitation, our study was limited in investigation with numerical simulations only. Provided the availability of resources, experimental investigations can be carried out. In experimental growth of self-organized nanowire array, merging of adjacent nanowires can be found. As the effects of such merging is not investigated in this study, further exploration of this can be interesting.
- We have explored the transmission gap that is identical to the TM bandgap of photonic crystals with similar diameter and areal fraction. The study can be extended to investigate the possibility of getting TE bandgap like transmission gaps also.

- Considering GaN to be the representative of dielectric materials, we have kept the refractive index of the material same throughout the study. Other dielectric materials can also be investigated.
- There is scope of further research to better understand the diameter dependence of scattering of light in the strongly disordered medium. In our analysis we have observed that both Bragg and Mie scattering play a role in strongly disordered media consisting of GaN nanowires. It will be interesting to investigate scattering phenomena in closer detail, particularly in disordered media comprising dielectric particles of different diameters and refractive indices.
- When the structural dimension is much smaller than the wavelength of EM wave, the structure can be thought of as a homogeneous medium with an effective refractive index and metamaterial effects arises in such structures [66]. As our considered diameters are comparable with the considered wavelengths, approximating these structures as a homogeneous material is not fully accurate. However, as the diameters are still slightly smaller than the visible portion of our wavelength range, further investigation can be carried out to compare our structures with metamaterials.
- For the inverse design, we have employed adjoint optimization and binary discretization techniques to generate the final designs. Other optimization and discretization techniques can be employed to find out the one providing the best performance.
- Disordered arrays are used for the realization of power splitters and wavelength demultiplexers only. Defining the objective function properly, optimized power combiner, multiplexers, waveguides, and photonic integrated circuits can be devised with such disordered nanowire arrays.

Bibliography

- [1] J. Caro, E. Roeling, B. Rong, H. M. Nguyen, E. Van Der Drift, S. Rogge, F. Karouta, R. W. van der Heijden, and H. Saleminck, “Transmission measurement of the photonic band gap of GaN photonic crystal slabs,” *Applied Physics Letters*, vol. 93, no. 5, p. 051117, 2008.
- [2] M. Bayindir, E. Cubukcu, I. Bulu, and E. Ozbay, “Photonic band-gap effect, localization, and waveguiding in the two-dimensional Penrose lattice,” *Phys. Rev. B*, vol. 63, p. 161104, Apr 2001. [Online]. Available: <https://link.aps.org/doi/10.1103/PhysRevB.63.161104>
- [3] J. D. Joannopoulos, S. G. Johnson, J. N. Winn, and R. D. Meade, *Photonic Crystals: Molding the Flow of Light - Second Edition*. Princeton University Press, 2011. [Online]. Available: <https://doi.org/10.1515/9781400828241>
- [4] D. W. Hahn, “Light scattering theory,” *Department of Mechanical and Aerospace Engineering, University of Florida*, 2009.
- [5] “Blue Sky, howpublished = <http://hyperphysics.phy-astr.gsu.edu/hbase/atmos/blusky.html>.”
- [6] Wikipedia contributors, “Bragg’s law — Wikipedia, the free encyclopedia,” https://en.wikipedia.org/w/index.php?title=Bragg%27s_law&oldid=1086971372, 2022, [Online; accessed 22-June-2022].
- [7] S. Jahangir, “III-Nitride self-assembled nanowire light emitting diodes and lasers on (001) Silicon.” Ph.D. dissertation, 2015.
- [8] K. Grossklauss, A. Banerjee, S. Jahangir, P. Bhattacharya, and J. Millunchick, “Misorientation defects in coalesced self-catalyzed GaN nanowires,” *Journal of crystal growth*, vol. 371, pp. 142–147, 2013.
- [9] D. J. Paul, A. A. Mimi, A. Hazari, P. Bhattacharya, and M. Z. Baten, “Finite-difference time-domain analysis of the tunability of Anderson localization of light in self-organized GaN nanowire arrays,” *Journal of Applied Physics*, vol. 125, no. 4, p. 043104, 2019.
- [10] K. Yee, “Numerical solution of initial boundary value problems involving Maxwell’s equations in isotropic media,” *IEEE Transactions on Antennas and Propagation*, vol. 14, no. 3, pp. 302–307, 1966.
- [11] “Stanford photonics inverse design software,” <https://web.stanford.edu/group/OTL/lagan/18012/SpinsOverview.pdf>.

- [12] E. Yablonovitch, “Inhibited spontaneous emission in solid-state physics and electronics,” *Phys. Rev. Lett.*, vol. 58, pp. 2059–2062, May 1987. [Online]. Available: <https://link.aps.org/doi/10.1103/PhysRevLett.58.2059>
- [13] F. Pommereau, L. Legouézigue, S. Hubert, S. Sainson, J.-P. Chandouineau, S. Fabre, G.-H. Duan, B. Lombardet, R. Ferrini, and R. Houdré, “Fabrication of low loss two-dimensional InP photonic crystals by inductively coupled plasma etching,” *Journal of Applied Physics*, vol. 95, no. 5, pp. 2242–2245, 2004. [Online]. Available: <https://doi.org/10.1063/1.1644630>
- [14] W. Man, M. Florescu, E. P. Williamson, Y. He, S. R. Hashemizad, B. Y. C. Leung, D. R. Liner, S. Torquato, P. M. Chaikin, and P. J. Steinhardt, “Isotropic band gaps and freeform waveguides observed in hyperuniform disordered photonic solids,” *Proceedings of the National Academy of Sciences*, vol. 110, no. 40, pp. 15 886–15 891, 2013. [Online]. Available: <https://www.pnas.org/doi/abs/10.1073/pnas.1307879110>
- [15] G. Wu, Z. Cai, J. Wang, and T. Nee, “Design and simulation in gan based light emitting diodes using focused ion beam generated photonic crystals,” *Surface and Coatings Technology*, vol. 203, no. 17, pp. 2674–2678, 2009, sMMIB-15. [Online]. Available: <https://www.sciencedirect.com/science/article/pii/S0257897209001923>
- [16] N. Vico Triviño, G. Rossbach, U. Dharanipathy, J. Levrat, A. Castiglia, J.-F. Carlin, K. Atlasov, R. Butté, R. Houdré, and N. Grandjean, “High quality factor two dimensional GaN photonic crystal cavity membranes grown on silicon substrate,” *Applied Physics Letters*, vol. 100, no. 7, p. 071103, 2012.
- [17] T.-C. Lu, S.-W. Chen, L.-F. Lin, T.-T. Kao, C.-C. Kao, P. Yu, H.-C. Kuo, S.-C. Wang, and S. Fan, “GaN-based two-dimensional surface-emitting photonic crystal lasers with AlN/GaN distributed Bragg reflector,” *Applied Physics Letters*, vol. 92, no. 1, p. 011129, 2008.
- [18] N. D. Gupta, V. Janyani, M. Mathew, M. Kumari, and R. Singh, “Design and fabrication of InGaN/GaN superlattice-based solar cell using photonic crystal structure,” *Journal of Nanophotonics*, vol. 12, no. 4, pp. 1 – 15, 2018. [Online]. Available: <https://doi.org/10.1117/1.JNP.12.043505>
- [19] C. Han, M. Kang, and H. Jeon, “Lasing at multidimensional topological states in a two-dimensional photonic crystal structure,” *ACS Photonics*, vol. 7, no. 8, pp. 2027–2036, 2020. [Online]. Available: <https://doi.org/10.1021/acsp Photonics.0c00357>
- [20] X. Tang, L. Han, Z. Ma, Z. Deng, Y. Jiang, W. Wang, H. Chen, C. Du, and H. Jia, “Enhanced light extraction from algainp-based red light-emitting diodes with photonic crystals,” *Opt. Express*, vol. 29, no. 4, pp. 5993–5999, Feb 2021. [Online]. Available: <http://opg.optica.org/oe/abstract.cfm?URI=oe-29-4-5993>
- [21] J. Buencuerpo, T. E. Saenz, M. Steger, M. Young, E. L. Warren, J. F. Geisz, M. A. Steiner, and A. C. Tamboli, “Efficient light-trapping in ultrathin gaas solar cells using quasi-random photonic crystals,”

- Nano Energy*, vol. 96, p. 107080, 2022. [Online]. Available: <https://www.sciencedirect.com/science/article/pii/S2211285522001628>
- [22] M. Zhao, Z. Yang, R. Zhang, J. Zheng, P. Xu, W. Zhang, S. Dai, R. Wang, and A. Majumdar, “High q chalcogenide photonic crystal nanobeam cavities,” *IEEE Photonics Technology Letters*, vol. 33, no. 11, pp. 525–528, 2021.
- [23] A. Della Villa, S. Enoch, G. Tayeb, V. Pierro, V. Galdi, and F. Capolino, “Band gap formation and multiple scattering in photonic quasicrystals with a penrose-type lattice,” *Physical review letters*, vol. 94, no. 18, p. 183903, 2005.
- [24] K. Wang, S. David, A. Chelnokov, and J. Lourtioz, “Photonic band gaps in quasicrystal-related approximant structures,” *Journal of Modern Optics*, vol. 50, no. 13, pp. 2095–2105, 2003.
- [25] Y. Chan, C. T. Chan, and Z. Liu, “Photonic band gaps in two dimensional photonic quasicrystals,” *Physical Review Letters*, vol. 80, no. 5, p. 956, 1998.
- [26] S. Li, Z.-J. Wang, L.-S. Chen, X. Sun, and T. F. George, “Collective behavior and disorder-induced resonator of random lasers,” *Applied Physics Letters*, vol. 86, no. 17, p. 171109, 2005.
- [27] F. Pratesi, M. Burrelli, F. Riboli, K. Vynck, and D. S. Wiersma, “Disordered photonic structures for light harvesting in solar cells,” *Optics express*, vol. 21, no. 103, pp. A460–A468, 2013.
- [28] M. H. Tahersima, K. Kojima, T. Koike-Akino, D. Jha, B. Wang, C. Lin, and K. Parsons, “Deep neural network inverse design of integrated photonic power splitters,” *Scientific Reports*, vol. 9, no. 1, p. 1368, Feb 2019. [Online]. Available: <https://doi.org/10.1038/s41598-018-37952-2>
- [29] S. Molesky, Z. Lin, A. Y. Piggott, W. Jin, J. Vucković, and A. W. Rodriguez, “Inverse design in nanophotonics,” *Nature Photonics*, vol. 12, no. 11, pp. 659–670, Nov 2018. [Online]. Available: <https://doi.org/10.1038/s41566-018-0246-9>
- [30] B.-S. Song, S. Noda, and T. Asano, “Photonic devices based on in-plane hetero photonic crystals,” *Science*, vol. 300, no. 5625, pp. 1537–1537, 2003.
- [31] Y. A. Vlasov, M. O’boyle, H. F. Hamann, and S. J. McNab, “Active control of slow light on a chip with photonic crystal waveguides,” *nature*, vol. 438, no. 7064, pp. 65–69, 2005.
- [32] T. Baba, N. Fukaya, and J. Yonekura, “Observation of light propagation in photonic crystal optical waveguides with bends,” *Electronics letters*, vol. 35, no. 8, pp. 654–655, 1999.
- [33] P. Villeneuve, S. Fan, S. Johnson, and J. Joannopoulos, “Three-dimensional photon confinement in photonic crystals of low-dimensional periodicity,” *IEE Proceedings-Optoelectronics*, vol. 145, no. 6, pp. 384–390, 1998.

- [34] R. D. Meade, A. Rappe, K. Brommer, J. Joannopoulos, and O. Alerhand, “Accurate theoretical analysis of photonic band-gap materials,” *Physical Review B*, vol. 48, no. 11, p. 8434, 1993.
- [35] K. M. Ho, C. Chan, C. Soukoulis, R. Biswas, and M. Sigalas, “Photonic band gaps in three dimensions: new layer-by-layer periodic structures,” *Solid State Communications*, vol. 89, no. 5, pp. 413–416, 1994.
- [36] E. Melo and M. Alayo, “Photonic band gaps of wurtzite GaN and AlN photonic crystals at short wavelengths,” *Photonics and Nanostructures-Fundamentals and Applications*, vol. 14, pp. 35–45, 2015.
- [37] M. Bayindir, E. Cubukcu, I. Bulu, T. Tut, E. Ozbay, and C. Soukoulis, “Photonic band gaps, defect characteristics, and waveguiding in two-dimensional disordered dielectric and metallic photonic crystals,” *Physical Review B*, vol. 64, no. 19, p. 195113, 2001.
- [38] M. Florescu, S. Torquato, and P. J. Steinhardt, “Complete band gaps in two-dimensional photonic quasicrystals,” *Physical Review B*, vol. 80, no. 15, p. 155112, 2009.
- [39] —, “Designer disordered materials with large, complete photonic band gaps,” *Proceedings of the National Academy of Sciences*, vol. 106, no. 49, pp. 20 658–20 663, 2009. [Online]. Available: <https://www.pnas.org/doi/abs/10.1073/pnas.0907744106>
- [40] C. Rockstuhl, U. Peschel, and F. Lederer, “Correlation between single-cylinder properties and bandgap formation in photonic structures,” *Optics letters*, vol. 31, no. 11, pp. 1741–1743, 2006.
- [41] S. Nojima, G. Kaneda, and K. Aizawa, “Quantitative isolation of band-gap formation mechanisms by randomizing the lattice arrangement in photonic crystals,” *Journal of Applied Physics*, vol. 113, no. 12, p. 123105, 2013.
- [42] S. Arafin, X. Liu, and Z. Mi, “Review of recent progress of III-nitride nanowire lasers,” *Journal of Nanophotonics*, vol. 7, no. 1, p. 074599, 2013.
- [43] M. De La Mata, X. Zhou, F. Furtmayr, J. Teubert, S. Gradečak, M. Eickhoff, A. F. i Morral, and J. Arbiol, “A review of MBE grown 0D, 1D and 2D quantum structures in a nanowire,” *Journal of Materials Chemistry C*, vol. 1, no. 28, pp. 4300–4312, 2013.
- [44] K. Li, X. Liu, Q. Wang, S. Zhao, and Z. Mi, “Ultralow-threshold electrically injected AlGaIn nanowire ultraviolet lasers on Si operating at low temperature,” *Nature nanotechnology*, vol. 10, no. 2, p. 140, 2015.
- [45] A. Hazari, M. Zunaid Baten, L. Yan, J. M. Millunchick, and P. Bhattacharya, “An InN/InGaIn/GaN nanowire array guided wave photodiode on silicon,” *Applied Physics Letters*, vol. 109, no. 19, p. 191102, 2016.
- [46] C. Zhao, N. Alfaraj, R. C. Subedi, J. W. Liang, A. A. Alatawi, A. A. Alhamoud, M. Ebaid, M. S. Alias, T. K. Ng, and B. S. Ooi, “III-nitride

- nanowires on unconventional substrates: From materials to optoelectronic device applications,” *Progress in Quantum Electronics*, vol. 61, pp. 1–31, 2018.
- [47] A. Aiello, A. H. Hoque, M. Z. Baten, and P. Bhattacharya, “High-gain silicon-based InGaN/GaN Dot-in-Nanowire array photodetector,” *ACS Photonics*, vol. 6, no. 5, pp. 1289–1294, 2019.
- [48] D. Wang, C. Huang, X. Liu, H. Zhang, H. Yu, S. Fang, B. S. Ooi, Z. Mi, J.-H. He, and H. Sun, “Highly uniform, self-assembled AlGaIn nanowires for self-powered solar-blind photodetector with fast-response speed and high responsivity,” *Advanced Optical Materials*, vol. 9, no. 4, p. 2000893, 2021.
- [49] A. Hazari, F. C. Hsiao, L. Yan, J. Heo, J. M. Millunchick, J. M. Dallesasse, and P. Bhattacharya, “1.3 μ m optical interconnect on silicon: A monolithic III-Nitride nanowire photonic integrated circuit,” *IEEE Journal of Quantum Electronics*, vol. 53, no. 4, pp. 1–9, 2017.
- [50] A. Y. Piggott, E. Y. Ma, L. Su, G. H. Ahn, N. V. Saprà, D. Vercauteren, A. M. Netherton, A. S. P. Khope, J. E. Bowers, and J. Vučković, “Inverse-designed photonics for semiconductor foundries,” *ACS Photonics*, vol. 7, no. 3, pp. 569–575, 2020. [Online]. Available: <https://doi.org/10.1021/acsphotonics.9b01540>
- [51] C. Dory, D. Vercauteren, K. Y. Yang, N. V. Saprà, A. E. Rugar, S. Sun, D. M. Lukin, A. Y. Piggott, J. L. Zhang, M. Radulaski, K. G. Lagoudakis, L. Su, and J. Vučković, “Inverse-designed diamond photonics,” *Nature Communications*, vol. 10, no. 1, p. 3309, Jul 2019. [Online]. Available: <https://doi.org/10.1038/s41467-019-11343-1>
- [52] H. Ma, J. Huang, K. Zhang, and J. Yang, “Arbitrary-direction, multichannel and ultra-compact power splitters by inverse design method,” *Optics Communications*, vol. 462, p. 125329, 2020. [Online]. Available: <https://www.sciencedirect.com/science/article/pii/S003040182030050X>
- [53] —, “Inverse-designed arbitrary-input and ultra-compact $1 \times n$ power splitters based on high symmetric structure,” *Scientific Reports*, vol. 10, no. 1, p. 11757, Jul 2020. [Online]. Available: <https://doi.org/10.1038/s41598-020-68746-0>
- [54] A. Chen, S. Chua, P. Chen, X. Chen, and L. Jian, “Fabrication of sub-100 nm patterns in SiO₂ templates by electron-beam lithography for the growth of periodic III–V semiconductor nanostructures,” *Nanotechnology*, vol. 17, no. 15, p. 3903, 2006.
- [55] J. Stodolka, D. Nau, M. Frommberger, C. Zanke, H. Giessen, and E. Quandt, “Fabrication of two-dimensional hybrid photonic crystals utilizing electron beam lithography,” *Microelectronic Engineering*, vol. 78-79, pp. 442–447, 2005, proceedings of the 30th International Conference on Micro and Nano-Engineering. [Online]. Available: <https://www.sciencedirect.com/science/article/pii/S0167931704005921>

- [56] X. Wang, J. Xu, X. Quan, Y. Li, Y. Wang, and X. Cheng, “Fast fabrication of silicon nanopillar array using electron beam lithography with two-layer exposure method,” *Microelectronic Engineering*, vol. 227, p. 111311, 2020. [Online]. Available: <https://www.sciencedirect.com/science/article/pii/S016793172030099X>
- [57] S. D. Hersee, A. K. Rishinaramangalam, M. N. Fairchild, L. Zhang, and P. Varangis, “Threading defect elimination in GaN nanowires,” *Journal of Materials Research*, vol. 26, no. 17, pp. 2293–2298, 2011.
- [58] W. Guo, M. Zhang, P. Bhattacharya, and J. Heo, “Auger recombination in III-Nitride nanowires and its effect on nanowire light-emitting diode characteristics,” *Nano Letters*, vol. 11, no. 4, pp. 1434–1438, 2011, pMID: 21366223. [Online]. Available: <https://doi.org/10.1021/nl103649d>
- [59] F. Furtmayr, M. Vielemeyer, M. Stutzmann, J. Arbiol, S. Estradé, F. Peirò, J. R. Morante, and M. Eickhoff, “Nucleation and growth of GaN nanorods on Si (111) surfaces by plasma-assisted molecular beam epitaxy - the influence of Si- and Mg-doping,” *Journal of Applied Physics*, vol. 104, no. 3, p. 034309, 2008. [Online]. Available: <https://doi.org/10.1063/1.2953087>
- [60] T. Stoica, E. Sutter, R. J. Meijers, R. K. Debnath, R. Calarco, H. Lüth, and D. Grützmacher, “Interface and wetting layer effect on the catalyst-free nucleation and growth of GaN nanowires,” *Small*, vol. 4, no. 6, pp. 751–754, 2008. [Online]. Available: <https://onlinelibrary.wiley.com/doi/abs/10.1002/sml.200700936>
- [61] T. Stoica, E. Sutter, and R. Calarco, “GaN and InN nanowires: growth and optoelectronic properties,” *Trends in Nanophysics*, pp. 73–96, 2010.
- [62] S. G. Johnson and J. D. Joannopoulos, “Block-iterative frequency-domain methods for Maxwell’s equations in a planewave basis,” *Optics express*, vol. 8, no. 3, pp. 173–190, 2001.
- [63] A. F. Oskooi, D. Roundy, M. Ibanescu, P. Bermel, J. D. Joannopoulos, and S. G. Johnson, “MEEP: A flexible free-software package for electromagnetic simulations by the FDTD method,” *Computer Physics Communications*, vol. 181, no. 3, pp. 687–702, 2010.
- [64] L. Su, D. Vercruyse, J. Skarda, N. V. Sapra, J. A. Petykiewicz, and J. Vučković, “Nanophotonic inverse design with SPINS: Software architecture and practical considerations,” *Applied Physics Reviews*, vol. 7, no. 1, p. 011407, 2020. [Online]. Available: <https://doi.org/10.1063/1.5131263>
- [65] C. Liu, M. V. Rybin, P. Mao, S. Zhang, and Y. Kivshar, “Disorder-immune photonics based on mie-resonant dielectric metamaterials,” *Phys. Rev. Lett.*, vol. 123, p. 163901, Oct 2019. [Online]. Available: <https://link.aps.org/doi/10.1103/PhysRevLett.123.163901>
- [66] Wikipedia contributors, “Metamaterial — Wikipedia, the free encyclopedia,” <https://en.wikipedia.org/w/index.php?title=Metamaterial&oldid=1093763696>, 2022, [Online; accessed 5-July-2022].